TREM2 regulates purinergic receptor-mediated calcium signaling and motility in human iPSC-derived microglia

Amit Jairaman[1]†, Amanda McQuade[2,3,4]†, You Jung Kang[5], Alberto Granzotto[2,6,7], Jean Paul Chadarevian[2], Sunil Gandhi[2], Ian Parker[1,2], Ian Smith[2], Shivashankar Othy[1,8], Hansang Cho[5,9], Mathew Blurton-Jones[2,3,8]*, Michael Cahalan[1,8]*

Affiliations:

[1] Department of Physiology & Biophysics, University of California, Irvine, CA 92697-4561, USA

[2] Department of Neurobiology & Behavior, University of California, Irvine, CA 92697, USA

[3] Sue and Bill Gross Stem Cell Research Center, University of California, Irvine, CA 92697, USA

[4] UCI Institute for Memory Impairments and Neurological Disorders, University of California, Irvine, CA 92697, USA

[5] Department of Mechanical Engineering and Engineering Science, Center for Biomedical Engineering and Science, University of North Carolina, Charlotte, NC 28223, USA

[6] Center for Advanced Sciences and Technology (CAST), University "G. d'Annunzio" of Chieti-Pescara, Chieti 66100, Italy

[7] Department of Neuroscience, Imaging, and Clinical Sciences (DNISC), University "G. d'Annunzio" of Chieti-Pescara, Chieti 66100, Italy

[8] Institute for Immunology, University of California, Irvine, CA 92697, USA

[9] Institute of Quantum Biophysics, Department of Biophysics, Sungkyunkwan University, 2066 Seobu-ro, Jangan-gu, Suwon-si, Gyeonggi-do 16419, Korea

† Equal contributions

* Co-corresponding authors: Michael D. Cahalan (mcahalan@uci.edu), Mathew Blurton-Jones (mblurton@uci.edu)

Key Words: microglia, motility, Alzheimer's disease, P2Y receptor, Ca^{2+} signaling, store-operated Ca^{2+} entry (SOCE), genetically encoded Ca^{2+} indicator

Abstract

The membrane protein TREM2 (Triggering Receptor Expressed on Myeloid cells 2) regulates key microglial functions including phagocytosis and chemotaxis. Loss-of-function variants of TREM2 are associated with increased risk of Alzheimer's disease (AD). Because abnormalities in Ca^{2+} signaling have been observed in several AD models, we investigated TREM2 regulation of Ca^{2+} signaling via genetic deletion in human induced pluripotent stem cell-derived microglia (iPSC-microglia). We found that iPSC-microglia lacking TREM2 (TREM2 KO) show exaggerated Ca^{2+} signals in response to purinergic agonists such as ADP that shape microglial injury responses. This ADP hypersensitivity, driven by increased expression of P2Y12 and P2Y13 receptors, results in sustained Ca^{2+} influx and alters cell motility and process extension in TREM2 KO microglia. In a "Ca^{2+} clamp" assay using iPSC-microglia expressing the genetically encoded Ca^{2+} probe, Salsa6f, we found that cytosolic Ca^{2+} tunes motility to a greater extent in TREM2 KO microglia. Despite showing greater overall displacement, TREM2 KO microglia exhibit reduced directional chemotaxis along ADP gradients. Accordingly, the chemotactic defect in TREM2 KO microglia was rescued by reducing cytosolic Ca^{2+} using a P2Y12 receptor antagonist. Our results show that loss of TREM2 confers a defect in microglial Ca^{2+} response to purinergic signals, suggesting a window of Ca^{2+} signaling for optimal microglial motility.

45 **Main Text**

46 **Introduction**

47 As the primary immune cells of the central nervous system, microglia survey their local
48 environment to maintain homeostasis and respond to local brain injury or abnormal neuronal
49 activity. Microglia are strongly implicated in several neurodevelopmental and neurodegenerative
50 diseases[1–7], warranting further study of human microglial dynamics. Purinergic metabolites (ATP,
51 ADP, UTP, UDP) in the brain constitute key signals driving microglial activation and chemotaxis[8–
52 11]. ATP released from both homeostatic and damaged cells is hydrolyzed locally by nucleosidases
53 such as the ectonucleotidase NTPDase1 (CD39) or pyrophosphatase NPP1 to produce ADP[12–14].
54 ADP is then detected by P2Y purinergic receptors on microglia, causing IP_3-dependent Ca^{2+}
55 release from the endoplasmic reticulum (ER) lumen. Ca^{2+} depletion from the ER in turn activates
56 ER STIM1 proteins to translocate proximally to puncta where closely apposed plasma membrane
57 (PM) Orai1 channels are activated. This mechanism underlies store-operated Ca^{2+} entry (SOCE)
58 in many cell types [15], including microglia[16–18].

59 Purinergic signaling is central to microglial communication with other brain cell types and
60 has been negatively correlated with the onset of Disease Associated Microglia (DAM)
61 transcriptional states [19–23]. P2Y12 and P2Y13 receptors are highly expressed by microglia and are
62 activated predominantly by ADP [14,24]. P2Y12 receptors are essential for microglial chemotaxis and
63 have been implicated in the microglial response to cortical injury[25,26], NLRP3 inflammasome
64 activation [27,28], neuronal hyperactivity and protection[25,29], and blood brain barrier maintenance
65 [30]. While purinergic receptors have been broadly identified as markers of microglial homeostasis,

66 mechanisms by which receptor expression may drive or maintain homeostatic microglial states
67 remain incompletely understood.

68 Neuroinflammatory pathologies are often associated with altered Ca^{2+} signaling[31].
69 Microglia, in particular, show altered Ca^{2+} responses in mouse models of Alzheimer's Disease (AD)
70 by mechanisms that are not fully understood[32–34]. Ca^{2+} responses to purinergic metabolites have
71 been extensively studied in cultured murine microglia, acute brain slices, and more recently in
72 anesthetized mice [8,10,32,35–37]. However, our understanding of how specific patterns of Ca^{2+} signals
73 in microglia correlate with and tune downstream microglial responses such as cell motility or
74 process extension remains incomplete. There is also a paucity of knowledge on how regulators
75 of purinergic Ca^{2+} signals in microglia might play a role in the dysregulation of Ca^{2+} signaling
76 associated with aging and neuroinflammation.

77 TREM2 encodes a cell surface receptor that binds a variety of ligands including various
78 lipids, apolipoprotein E (ApoE), and amyloid-β peptides and signals through its adaptor protein
79 DAP12 to activate a host of downstream pathways[21,38–40]. Loss of TREM2 function is thought to
80 lock microglia in a more homeostatic-like state[21,41,42]. Indeed, microglia lacking TREM2 expression
81 fail to activate against disease pathology, correlating with increased risk of AD[21,39,43]. Purinergic
82 receptor hyperexpression has been reported at the transcriptome level across multiple TREM2
83 loss of function models including human patient mutations [19–21,23,39,44], although the mechanistic
84 link between purinergic receptor expression and TREM2 function remains poorly understood.

85 We previously developed methods to generate human induced pluripotent stem cell-
86 derived microglia (iPSC-microglia) [45,46], which can be used to model human microglial behavior *in*
87 *vitro*. While iPSC-microglia are proving increasingly useful to investigate neurodegenerative

88 disorders [47–51], Ca^{2+} signaling has not yet been extensively profiled in these models. In this study,
89 we examined purinergic Ca^{2+} signaling in human iPSC-microglia and found that sustained Ca^{2+}
90 influx in response to ADP regulates microglial process extension, motility speed, and turning
91 behavior. We show that microglia lacking TREM2 are hyperresponsive to purinergic signaling.
92 Using novel iPSC-microglia lines that express a ratiometric genetically encoded Ca^{2+} probe,
93 Salsa6f [52], we found that the motility characteristics of human wild-type and TREM2-knockout
94 microglia are differentially tuned by Ca^{2+} signaling. Informed by these discoveries, we were able
95 to rescue chemotactic deficiencies in TREM2-knockout microglia by dampening purinergic
96 receptor signaling.
97

98 **Results**

99 **Purinergic receptor Ca^{2+} signaling is enhanced in TREM2-knockout human iPSC-microglia**

100 To determine if TREM2 plays a role in microglial Ca^{2+} signaling, we compared cytosolic Ca^{2+}
101 responses to the purinergic agonist ADP in isogenic, CRISPR-modified wild type (WT) and TREM2-
102 knockout (TREM2 KO) human induced pluripotent stem cell-derived microglia (iPSC-microglia).
103 ADP stimulation induced a biphasic Ca^{2+} response – a rapid initial peak followed by sustained Ca^{2+}
104 elevation lasting several minutes, in line with previous observations in mouse microglia [53,54]. Both
105 phases of the Ca^{2+} response were significantly elevated in TREM2 KO microglia (**Figure 1A, B**).
106 TREM2 KO microglia also showed exaggerated Ca^{2+} responses to other purinergic agonists; ATP
107 and UTP (**Figure 1C, D**). Notably, responses to ATP and UTP decayed faster than responses to ADP
108 in both WT and TREM2 KO cells, indicating that purinergic stimulation by ADP is more potent in
109 inducing sustained Ca^{2+} signals in human iPSC-microglia (**Figure 1E and Figure 1-figure**
110 **supplement 1A**).

111

112 **Sustained ADP-evoked Ca^{2+} elevation in TREM2 KO microglia is not due to SOCE enhancement**

113 To determine the mechanism driving higher ADP-evoked Ca^{2+} signals observed in TREM2 KO cells,
114 we investigated the individual steps in the purinergic Ca^{2+} signaling pathway. The initial Ca^{2+}
115 response to P2Y receptor engagement occurs through phospholipase C and IP_3-mediated ER Ca^{2+}
116 store-release, which triggers sustained cytosolic Ca^{2+} elevation by SOCE (**Figure 1F**). Consistent
117 with this, the sustained Ca^{2+} phase in TREM2 KO iPSC-microglia was blocked by Gd^{3+} and 2-APB,
118 non-specific inhibitors of SOCE (**Figure 1-figure supplement 1B**). To determine if SOCE is
119 increased in TREM2 KO microglia, we directly measured the rate of Ca^{2+} influx following Ca^{2+} re-

120 addition after maximal store-depletion by the SERCA pump inhibitor, thapsigargin (TG). Instead,
121 we find the rate and amplitude of SOCE were both modestly reduced in TREM2 KO cells (**Figure**
122 **1G**), and thus changes in the maximal capacity of SOCE do not account for the elevated response
123 of TREM2 KO microglia to ADP. Moreover, STIM1 and Orai1 mRNA expression, and Orai1 protein
124 expression are similar in WT and TREM2 KO microglia (**Figure 1-figure supplement 2**).
125 We therefore hypothesized that the exaggerated secondary Ca^{2+} phase in TREM2 KO
126 microglia may be driven primarily by increased ER Ca^{2+} store-release resulting in increased SOCE.
127 To assess this, we plotted Ca^{2+} responses in individual cells, using Ca^{2+} levels 5 min after ADP as
128 a surrogate for SOCE engagement and the initial peak Ca^{2+} as a readout of ER store-release (**Figure**
129 **1-figure supplement 3**). Both WT and TREM2 KO microglia showed a similar relationship between
130 SOCE and store-release, suggesting that SOCE is engaged by similar mechanisms in the two cell
131 types, but is recruited to a greater extent in TREM2 KO cells due to increased ER store-release.
132 To examine whether a larger ER store content contributes to increased Ca^{2+} responses in TREM2
133 KO microglia, we measured Ca^{2+} levels after maximally depleting ER stores with thapsigargin (TG),
134 ionomycin, or by IP_3 uncaging in Ca^{2+}-free solution buffered with EGTA. In all instances,
135 quantification of peak or cumulative cytosolic Ca^{2+} increase suggested that ER store-content and
136 IP_3 receptor activity is not altered in microglia lacking TREM2 (**Figure 1G-I**). These results indicate
137 that TREM2 controls ADP-driven Ca^{2+} signals upstream of IP_3 receptors, ER Ca^{2+} store levels, and
138 SOCE.
139
140 **Up-regulated P2Y12 and P2Y13 receptor expression drives increased ER Ca^{2+} release in TREM2-**
141 **KO microglia**

142 To isolate the early events of Ca^{2+} signaling upstream of SOCE, we monitored Ca^{2+} store release
143 in Ca^{2+}-free medium and found that TREM2 KO cells still showed significantly higher Ca^{2+} response
144 to ADP, compared to WT (**Figure 2A, B**). Dose-response curves for the peak Ca^{2+} response showed
145 a steep leftward shift in TREM2 KO cells (**Figure 2C**). The EC_{50} value for WT microglia was 650 nM,
146 whereas TREM2 KO microglia reached their EC_{50} by 15 nM. This stark difference was driven at
147 least in part by a diminished percentage of WT cells responding to ADP at low μM doses (**Figure**
148 **2D**). However, limiting the analysis to only those cells that show a Ca^{2+} rise revealed that
149 responding TREM2 KO cells still exhibited higher Ca^{2+} responses to ADP than "responding" WT
150 cells (**Figure 2E**). TREM2 KO microglia are thus significantly more sensitive to ADP than WT cells
151 and exhibit a strong shift in dose-dependent response which may be critical in sensing ADP and
152 in detecting ADP gradients.

153 In principle, signal amplification in microglia lacking TREM2 could occur at the level of P2Y
154 receptors or IP_3 receptors. Our results with IP_3 uncaging (**Figure 1I**) rule out any major differences
155 in IP_3 receptor expression or activity. This was further corroborated at the transcriptome level,
156 which showed similar expression of IP_3 receptor type 2 (the major IP_3R subtype expressed in iPSC-
157 microglia) mRNA in WT and TREM2 KO cells (**Figure 1-figure supplement 2**)[39,45]. We therefore
158 focused on P2Y12 and P2Y13 receptors, the main P2Y receptor subtypes in microglia that bind
159 ADP[45,46]. RNA sequencing showed that expression of P2Y12 and P2Y13 receptors was significantly
160 increased in TREM2 KO cells (**Figure 2F**). To confirm up-regulation at the protein level, we
161 performed immunostaining and found significantly higher expression of both these receptors on
162 the PM of TREM2 KO cells (**Figure 2G, H**). Consistent with this, Ca^{2+} responses to ADP in Ca^{2+} free
163 medium were significantly inhibited by P2Y12 and P2Y13 receptor antagonists (PSB 0739 and

164 MRS 2211) in both WT and TREM2 KO microglia (**Figure 2I, J**), implicating involvement of both
165 receptor subtypes. In summary, deletion of TREM2 in iPSC-derived microglia leads to up-
166 regulation of P2Y12 and P2Y13 receptors, rendering the cells hypersensitive to ADP signaling.
167

168 **ADP potentiates cell motility and process extension in human WT iPSC-microglia**

169 ADP is a potent chemoattractant for microglia [10]. Analogous to a previous study in fibroblasts [55],
170 we found that ADP treatment alters cell motility and leads to increased rates of scratch wound
171 closure in WT iPSC-microglia (**Figure 3A**). To investigate the cellular mechanism of accelerated
172 wound closure, we used time-lapse imaging to track open-field microglial cell motility (**Figure 3B**).
173 Mean cell speed and displacement (defined as the overall change in position from the origin at a
174 given time) were both increased after application of ADP, whereas average track straightness
175 was unaltered (**Figure 3C**). These data suggest that ADP-driven changes in motility in WT iPSC-
176 microglia primarily arise from increases in microglial speed, not altered turning behavior. ADP-
177 dependent increases in speed were reversed in the presence of P2Y12 (PSB 0739) and P2Y13
178 (MRS 2211) receptor antagonists, confirming the role of ADP in microglial cell motility (**Figure**
179 **3D**). To determine if Ca^{2+} influx regulates ADP-mediated increases in motility, we measured cell
180 migration with ADP in Ca^{2+}-free medium; in this paradigm, a transient Ca^{2+} signal would result
181 from P2Y receptor-induced IP_3 generation and release of Ca^{2+} from internal stores, but without
182 Ca^{2+} entry across the PM. We found that removing extracellular Ca^{2+} significantly decreased cell
183 speed, displacement, and track straightness (**Figure 3E**).

184 In addition, some microglia responded to ADP addition by extending processes and
185 altering their morphology rather than increasing motility (**Figure 3-figure supplement 1**).

186 Microglia have been observed to extend processes in response to injury and purinergic
187 stimulation in brain slices [8,26]. Therefore, we compared process complexity before and 30 min
188 after ADP exposure in WT microglia and observed significant increases in both the number of
189 branches per process and total length of these processes (**Figure 3F**). Similar to effects on cell
190 motility, ADP-mediated process extension was inhibited by P2Y12 (PSB 0739) and P2Y13 (MRS
191 2211) receptor antagonists. Furthermore, even before process extension was activated with ADP,
192 cells treated with P2Y antagonists showed significantly fewer and shorter processes. Altogether,
193 these results demonstrate that Ca^{2+} influx across the PM is required for optimal ADP-induced
194 migration and extension of processes in WT iPSC-microglia.
195
196 **ADP-evoked changes in cell motility and process extension are enhanced in TREM2-KO**
197 **microglia**
198 To characterize differences in motility characteristics between WT and TREM2 KO microglia
199 responding to ADP, we plotted mean squared displacement (MSD) vs time and compared cell
200 track overlays (flower plots) which showed that ADP enhances motility in TREM2 KO cells to a
201 greater extent than in WT microglia (**Figure 4A, B**). Baseline motility characteristics in
202 unstimulated cells, however, were similar in WT and TREM2-KO cells (**Figure 4-figure supplement**
203 **1A-C**), consistent with our previously published findings showing no difference in scratch wound
204 closure rates [39]. To further understand the basis of differences in ADP-induced motility between
205 WT and TREM2 KO cells, we analyzed mean speed, displacement and track straightness. Although
206 mean speeds were similar, TREM2 KO microglia showed greater displacement than WT cells
207 (**Figure 4C, D**), raising the possibility that KO cells may turn with lower frequency. Indeed, an

208 analysis of track straightness revealed that TREM2 KO microglia move farther from their origin
209 for the same total distance traveled (**Figure 4E**). Vector autocorrelation, an analysis of directional
210 persistence [57], further confirmed that WT cells turn more frequently than TREM2 KO microglia
211 (**Figure 4-figure supplement 1D, E**). To assess if these differences in TREM2 KO cells require
212 sustained Ca^{2+} influx, we analyzed microglial motility in response to ADP stimulation in the
213 absence of extracellular Ca^{2+} (**Figure 4F-J**). Mean-squared displacement (MSD) and cell-track
214 overlay plots showed that motility is constrained when Ca^{2+} is removed from the external bath in
215 both WT and TREM2 KO cells (**Figure 4 A, B vs. F, G**). In the absence of extracellular Ca^{2+}, TREM2
216 KO microglia showed similar mean speed, displacement, and track-straightness as WT cells
217 (**Figure 4 C-E vs H-J**). We conclude that increases in microglial motility (speed, displacement, and
218 straightness) require sustained Ca^{2+} influx, and that deletion of TREM2 reduces microglial turning
219 in response to ADP.

220 We next analyzed how TREM2 deletion affects the extension of cellular processes.
221 Compared to WT cells, TREM2 KO iPSC-microglia showed a more dramatic increase in the number
222 of branches and length of processes extended in response to ADP (**Figure 4 K-M, Figure 4-figure**
223 **supplement 2A, B**). Some of these differences can be attributed to the reduced morphological
224 complexity of TREM2 KO cells prior to stimulation. Importantly, Ca^{2+} entry across the PM is
225 required in WT microglia for optimal process extension in response to ADP, since ADP stimulation
226 in Ca^{2+}-free medium was insufficient to induce process extension (**Figure 4-figure supplement 2A**
227 **and B vs C and D**). However, TREM2 KO cells still showed some increase in process branching and
228 extension following ADP addition in the absence of external Ca^{2+} (**Figure 4-figure supplement 2C,**

229 **D**). Together, these results indicate that the increase in Ca^{2+} influx regulates microglial motility
230 and process extension to a greater extent in TREM2 KO microglia.
231
232 **Expression of Salsa6f, a ratiometric Ca^{2+} reporter, does not perturb microglial functions**
233 Our findings so far suggest that patterns of Ca^{2+} signaling in iPSC-microglia regulate cell motility
234 and process extension. To further characterize the effects of sustained Ca^{2+} signals on microglia
235 motility, we developed a novel iPSC line that expresses a genetically encoded, ratiometric Ca^{2+}
236 indicator, Salsa6f, to monitor cytosolic Ca^{2+} and motility simultaneously in individual cells [52].
237 Salsa6f relies on GCaMP6f to detect Ca^{2+}, which is fused with tdTomato in order to provide a
238 stable Ca^{2+}-independent red fluorescence, allowing cells to be tracked consistently even when
239 Ca^{2+} levels are low. Salsa6f WT iPSC-microglia showed the expected increase in the GCaMP6f
240 fluorescence in response to Ca^{2+} elevation without affecting tdTomato signal, permitting
241 determination of ratiometric Ca^{2+} levels (G/R ratio), and confirming that the probe was functional
242 (**Figure 5A-C and Figure 5-figure supplement 1**). Compared to non-transgenic iPSC-microglia,
243 Salsa6f-expressing cells showed similar expression of microglial identity markers P2RY13 and
244 IBA1, retained their ability for phagocytosis across several substrates, and had similar
245 differentiation yields, indicating that Salsa6f expression does not perturb microglial function or
246 activation (**Figure 5D-G**). Isogenic Salsa6f-lines lacking TREM2 were more responsive to ADP than
247 WT cells, consistent with our data in Figures 1 and 2 (**Figure 5H**). Using this model, we were able
248 to simultaneously track Ca^{2+} signals and cell-motility in response to ADP (**Figure 5I**).
249
250 **Ca^{2+} levels tune motility in TREM2 KO iPSC-microglia**

251 To isolate the specific effects of sustained Ca^{2+} elevations on microglia motility, we developed a
252 "Ca^{2+} clamp" protocol that relies on triggering SOCE and varying external Ca^{2+} to stabilize cytosolic
253 Ca^{2+} at "low" or "high" levels in the Salsa6f reporter line (**Figure 6A**), similar to our previous study
254 in T lymphocytes [59]. ER Ca^{2+} stores were depleted by addition of TG in Ca^{2+}-free medium, followed
255 by readdition of 0.2 or 2 mM external Ca^{2+} (**Figure 6B**). Motility measurements were made during
256 the slowly-falling phase of the Ca^{2+} response (**Figure 6C**). In WT cells, lowering extracellular Ca^{2+}
257 from 2 to 0.2 mM predictably decreased the G/R ratio but did not influence mean speed, cell
258 displacement, or track straightness (**Figure 6C, D top**). However, in TREM2 KO microglia, clamping
259 Ca^{2+} to a lower level significantly increased speed, displacement, and track straightness (**Figure**
260 **6C, D bottom**). These data suggest that motility characteristics of TREM2 KO microglia are more
261 sensitive to changes in cytoplasmic Ca^{2+} levels than in WT cells. Addition of ADP in this "clamp"
262 paradigm to activate Ca^{2+}-independent signaling pathways that regulate cell motility did not alter
263 the potential for Ca^{2+} to tune cell motility in TREM2 KO microglia (**Figure 6-figure supplement**
264 **1A**).

265 To further analyze the Ca^{2+} dependence of microglial motility, we plotted Salsa6f G/R Ca^{2+}
266 ratios at every time point against the instantaneous speeds for each individual cell (**Figure 6E**).
267 These data revealed a stronger dependence of instantaneous speed on Ca^{2+} levels in TREM2 KO
268 microglia (**Figure 6F**). Furthermore, when stratifying cell speed arbitrarily as "fast" (> 10 μm/min)
269 or "slow" (< 10 μm /min), we observe a marked reduction in the percentage of "fast" cells when
270 Ca^{2+} levels are high in TREM2 KO microglia (**Figure 6G**). Interestingly, cell displacement correlated
271 with Ca^{2+} to the same degree in both WT and KO cells (**Figure 6-figure supplement 1B, C**).

272 Together, the Ca^{2+} clamp experiments show that TREM2 KO human microglia are more sensitive
273 to tuning of motility by cytosolic Ca^{2+} than WT cells.
274
275 **Chemotactic defects in TREM2 KO microglia are rescued by dampening purinergic receptor**
276 **activity**
277 *In vivo,* directed migration of microglia is driven by gradients of ADP from dying or injured cells
278 [26,29]. To study chemotaxis toward ADP over a stable gradient, we exposed iPSC-microglia to ADP
279 in two-chamber microfluidic devices. Consistent with previous findings, WT iPSC-microglia
280 directionally migrated up the concentration gradient of ADP resulting in higher numbers of cells
281 within the central chamber [39,60]. In the absence of a chemotactic cue, this directional migration
282 was lost (**Figure 7A**). This assay revealed a deficit of chemotaxis in TREM2 KO microglia (**Figure**
283 **7A**), mirroring reports that TREM2 KO microglia are unable to migrate toward damaged neurons
284 near amyloid plaques in AD[38,39,61]. Given that ADP hypersensitivity in TREM2 KO cells is driven by
285 increased expression of P2Y receptors, we examined the effects of dampening P2Y signaling to
286 WT levels. Treatment with the P2Y12 antagonist, PSB 0739, reduced Ca^{2+} responses in TREM2 KO
287 cells and rescued the migration deficit in the chemotaxis assay (**Figure 7B-C)**. These results link
288 the increased Ca^{2+} signals and altered motility characteristics evoked by ADP in TREM2 KO cells
289 to directed migration toward areas of tissue damage, a vital functional response in microglia.
290

291 **Discussion**

292 This study focuses on two aims: understanding the roles of purinergic signaling in regulating
293 human microglial motility behavior; and elucidating the impact of TREM2 loss of function on this
294 pathway. We find that the high level of purinergic receptor expression in TREM2 KO iPSC-
295 microglia renders them highly sensitive to ADP-mediated signaling and leads to exaggerated
296 cytoplasmic Ca^{2+} responses. Mechanistically, this increase in Ca^{2+} signals is driven by enhanced
297 IP_3-mediated store-release coupled to SOCE. Indeed, based on the dose-response curves for peak
298 ADP-Ca^{2+} responses in Ca^{2+} free buffer, TREM2 KO cells have an EC_{50} at least 10-fold lower than
299 WT cells. As a functional consequence, TREM2 KO microglia exhibit a defect in turning behavior.
300 Despite moving in straighter paths, TREM2 KO cells are unable to migrate towards a gradient of
301 ADP as efficiently as WT cells, concordant with previous studies showing reduced migration of
302 TREM2 KO cells towards Aβ plaques[39]. We propose a model (**Figure 8**) whereby enhanced ADP
303 signaling abolishes the ability of TREM2 KO cells to distinguish gradations of agonist (in this case
304 ADP). The loss of gradient-sensing results in an inability to perform directed migration. We
305 hypothesize that increased ADP signaling and exaggerated Ca^{2+} responses in TREM2 KO cells
306 result in Ca^{2+} signaling domains that are no longer restricted to the cell region near to the highest
307 ADP concentrations, thereby disrupting the polarity of key signaling molecules that drive directed
308 cell motility.

309 The amplitude and duration of Ca^{2+} signals shape specificity of downstream cell
310 responses. Our experiments with ADP in Ca^{2+} free medium revealed that a transient Ca^{2+} signal
311 is insufficient to induce microglial motility in either WT or TREM2 KO cells. Previous studies have
312 shown that mouse microglia with genetic deletion of STIM1 or Orai1 also show defects in cell

313 migration to ATP[53,62], likely because diminished SOCE renders them unable to sustain Ca^{2+} signals
314 in response to ATP. The dependence of motility on prolonged purinergic Ca^{2+} signals may thus be
315 a general feature of microglia. In contrast, a Ca^{2+} transient can initiate some process extension in
316 TREM2 KO but not in WT microglia, suggesting a threshold for ADP signaling that is reached in KO
317 but not WT cells, and highlighting subtle differences in the Ca^{2+} requirement for motility and
318 process extension in TREM2 KO microglia.

319 To directly monitor Ca^{2+} signaling and motility simultaneously in individual cells, we
320 developed a novel iPSC-microglia cell-line expressing a genetically encoded, ratiometric Ca^{2+}
321 indicator Salsa6f, a GCaMP6f-tdTomato fusion protein. Because Salsa6f allows simultaneous
322 measurement of Ca^{2+} signal and tracking of processes, this Salsa6f iPSC line is likely to be a useful
323 tool to dissect the relationship between Ca^{2+} signaling and the function of various iPSC-derived
324 human cell types including neurons, astrocytes, and microglia. In addition, this line may be readily
325 xenotransplanted for use with human/microglia chimeric models to examine functional Ca^{2+}
326 responses to injury and pathology *in vivo*. Using Salsa6f-expressing microglia, we uncovered
327 critical differences in how Ca^{2+} levels tune motility in WT and TREM2 KO microglia. By tracking
328 instantaneous velocity at the same time as Salsa6f Ca^{2+} ratios in individual cells, we found that
329 TREM2 KO cell motility showed a greater sensitivity to changes in cytosolic Ca^{2+} levels with
330 significantly higher speeds than WT cells at lower Ca^{2+} and a more dramatic reduction in cell
331 speed at high Ca^{2+} levels. Accordingly, reducing cytosolic Ca^{2+} in a Ca^{2+} "clamp" assay resulted in
332 increased mean speed, displacement, and straighter paths for TREM2 KO iPSC-microglia, but had
333 no effect on these motility metrics in WT cells. Consistent with this observation, chemotaxis in
334 TREM2 KO cells was restored by partially inhibiting P2RY12 receptors. In response to

335 neurodegenerative disease, microglia down-regulate P2RY12[21,23,30]. Active regulation of
336 purinergic receptor expression is critical for sensing ADP gradients and decreasing motility near
337 the chemotactic source. Further understanding of how TREM2 KO cells dysregulate purinergic
338 receptor expression after an insult may prove useful for therapeutic modulation of microglial
339 activation states.

340 The studies presented here provide evidence that reducing purinergic receptor activity
341 may be clinically applicable in Alzheimer's patients with TREM2 loss of function mutations [38,50,63].
342 Pharmacologically targeting P2Y12 receptors to dampen both the Ca^{2+} dependent (PLC) and
343 independent (DAG) arms of the GPCR signaling pathway may be useful to control microglial
344 activation and motility. However, our results suggest that altering downstream Ca^{2+} flux may be
345 sufficient, and thus CRAC (Orai1) channel blockers that would specifically inhibit the sustained
346 Ca^{2+} signals without affecting the initial Ca^{2+} transient or the activation of DAG may provide a
347 more targeted approach.

348 Currently, TREM2 activating antibodies are being examined in early stage clinical trials for
349 Alzheimer's disease[64,65], making it critically important to understand the broad consequences of
350 TREM2 signaling. Therefore, an understanding of how TREM2 influences responses to purinergic
351 signals, and regulates cytosolic Ca^{2+} in human iPSC-microglia is critical. Beyond TREM2, we have
352 found that protective variants in MS4A6A and PLCG2 gene expression also decrease P2Y12 and
353 P2Y13 receptor expression (unpublished data), suggesting this mechanism of microglial
354 activation could be common to several microglial AD risk loci.

355 In summary, deletion of TREM2 renders iPSC-microglia highly sensitive to ADP, leading to
356 prolonged Ca^{2+} influx which increases cell displacement by decreasing cell turning. Despite this,

357 TREM2 KO microglia show a defect in chemotaxis that is likely due to their inability to sense ADP
358 gradients. Decreasing purinergic signaling in TREM2 KO microglia is able to rescue directional
359 chemotactic migration. We suggest that purinergic modulation or direct modulation of Ca^{2+}
360 signaling could provide novel therapeutic strategies in many AD patient populations, not solely
361 those with reduced TREM2 function.
362
363 **Figure Legends**
364
365 **Figure 1: Microglia lacking TREM2 show exaggerated Ca^{2+} responses to purinergic stimulation.**
366 (**A**) Representative images of WT (top) and TREM2 KO (bottom) iPSC-microglia loaded with Fluo-
367 4 (green) and Fura-red (red) showing resting cytosolic Ca^{2+} and peak Ca^{2+} after ADP addition.
368 Bright-field image overlaid, scale bar= 20 μm. (**B-D**) Average ratiometric traces (left panels)
369 showing changes in cytosolic Ca^{2+} over time in response to 2.5 μM ADP (**B**), 2.5 μM ATP (**C**), and
370 10 μM UTP (**D**) in 1 mM Ca^{2+} containing buffer (n=39-44 cells, **B**; 63-71 cells, **C**; 45-55 cells, **D**).
371 Quantification of baseline subtracted peak Ca^{2+} response and cytosolic Ca^{2+} levels 5 min after
372 agonist application shown on the right (250-274 cells, **B**; 165-179 cells, **C**; 175-269 cells, **D**; 3-5
373 experiments; Mann-Whitney test). (**E**) Ca^{2+} levels in WT iPSC-microglia 5 min after addition of
374 ADP, ATP, and UTP (right, n=17-52 cells from 2-3 experiments). Cells were gated for similar initial
375 peak Ca^{2+} response to agonists (left). (**F**) Schematic highlighting key downstream Ca^{2+} signaling
376 events in response to ADP. (**G**) Average trace showing SOCE engaged via emptying ER Ca^{2+} stores
377 with thapsigargin (TG, 2 μM) in Ca^{2+}-free buffer followed by re-addition of 1 mM Ca^{2+} (90-129
378 cells). Bar-graph summaries of ER store-release quantified as area under the curve, rate of SOCE,
379 and peak SOCE (187-266 cells, 2 experiments, Mann-Whitney test). (**H**) Average trace (left, 71-
380 117 cells) and summary of ER store-release after 2 μM ionomycin treatment in Ca^{2+} free buffer
381 (right, 146-234 cells, 2 experiments; Mann-Whitney test) (**I**) Same as H but in response to UV IP_3
382 uncaging (167-200 cells, nonparametric t-test). Data shown as mean ± SEM for traces and bar-
383 graphs.
384

385 **Figure 2: Higher sensitivity of TREM2 KO microglia to ADP is driven by increased purinergic**
386 **receptor expression**
387 (**A**) Representative images of WT (top) and TREM2 KO (bottom) iPSC-microglia before and peak
388 Ca^{2+} response after ADP addition in Ca^{2+} free buffer. Overlay of Fluo-4 (green), Fura-red (red) and
389 Brightfield (grey) images. Scale bar= 20 μm. (**B**) Average trace showing Ca^{2+} response to ADP in
390 Ca^{2+}-free buffer (left, 64-83 cells). Quantification of peak signal (right, 264-289 cells, 4
391 experiments, Mann-Whitney test). (**C-E**) Dose-response curve showing baseline subtracted Peak
392 Ca^{2+} responses to ADP in Ca^{2+}-free buffer (**C**), percent of "responding" cells (**D)** and peak Ca^{2+}
393 responses only in "responding" cells (**E**). (Each data-point is average of 84-474 cells, WT; 70-468
394 cells, 2-5 experiments). (**F**) RNA normalized read counts of P2RY12/13 expression from bulk RNA-
395 sequencing of WT and TREM2 KO iPSC-microglia (n=4, adjusted p-values from DESeq2). (**G-H**)
396 Immunofluorescence and quantification of P2RY12 (**G**) and P2RY13 (**H**) in iPSC-microglia (n=4
397 independent wells, 3 images per well, student's t-test). (**I-J**) Peak Ca^{2+} response in Ca^{2+} free buffer
398 after treatment with ADP in the presence of P2RY12 antagonist PSB 0739 (**I**) and P2RY13
399 antagonist MRS 2211 (**J**). (72-128 cells, **I**; 83-117 cells, **J**; representative of 3 experiments, Mann-
400 Whitney Test). Data shown as mean ± SEM for traces and bar-graphs.
401
402 **Figure 3: Nondirectional ADP exposure increases WT microglial speed and process extension.**
403 (**A**) Average trace showing closure of scratch wound produced with IncuCyte S3 WoundMaker.
404 iPSC-microglia imaged every 30 min after scratch wound with or without ADP stimulation (n=4
405 wells; 2 images per well). (**B**) Representative image of WT iPSC-microglia motility 30 min after
406 ADP exposure with cell tracks overlain (left). Pseudocolored images (center) across time: 0 min
407 (red), 4 min (orange), 8 min (yellow), 12 min (green), 16 min (cyan), 20 min (blue), 24 min (purple),
408 28 min (magenta). Scale bar= 100 μm. White boxes zoomed in at right to demonstrate motile
409 (top) and non-motile (bottom) cells. (**C**) Representative color images (top left) and displacement
410 vectors (bottom left) of WT iPSC-microglia at baseline (no ADP, grey) and 30 min after 2.5 μM
411 ADP treatment (red). Summary of Mean Speed (μm/min), Displacement over 10 min (μm/10 min)
412 and Track straightness (track length/track displacement) (414-602 cells, 2 experiments). (**D**)
413 Representative images, displacement vectors, and quantification of WT iPSC-microglia motility

414 for 20 min following ADP addition. Cells were pre-treated with vehicle (grey), MRS 2211 (10 μM,
415 gold), or PBS 0739 (10 μM, blue) (180-187 cells, 2 experiments). (**E**) Representative images,
416 displacement vectors, and quantification of WT iPSC-microglia motility after ADP in 1 mM Ca^{2+}
417 (light grey) or Ca^{2+}-free buffer (dark grey) (401-602 cells, 3 experiments). (**F**) Representative
418 images (left) and process extension (right) of iPSC-microglia (cytoplasmic GFP, grey) before or 30
419 min after ADP addition. Cells were pre-treated with vehicle (grey), MRS 2211 (10 μM, gold), or
420 PBS 0739 (10 μM, blue) (52-163 cells, 3-4 experiments). (**C-F**) One way ANOVA with Tukey post
421 hoc test. Data shown as mean ± SEM for traces and bar-graphs.
422
423 **Figure 4: ADP-driven process extension and cell displacement are increased in TREM2 KO iPSC-**
424 **microglia.** (**A-E**) Motility of WT (grey) and TREM2 KO (green) iPSC-microglia over 20 min following
425 ADP addition in 1 mM Ca^{2+}-containing buffer. (**A**) Plots of track displacement in μm centered from
426 point of origin at (0,0). (**B**) Mean-squared displacement (MSD) vs time. Mean-cell speeds (**C**), total
427 track displacement in 10-min interval (**D**), and track straightness (**E**) for 130-327 cells, 7
428 experiments, student's t-test. (**F-J**). Same as (**A-F**) but in Ca^{2+}-free medium (125-279 cells, 2
429 experiments, student's t-test). (**K**) Representative images of GFP-expressing WT (top) and TREM2
430 KO (bottom) iPSC-microglia, before and 30 min after 2.5 μM ADP addition. (**L**) Quantification of
431 total number of branches per cell before and after ADP treatment (left) and paired dot-plots
432 showing fold change in branch number from pre-ADP levels (right). Each data-point represents
433 an imaging field in the paired-plots. (**M**) Total process length before and after ADP treatment
434 displayed as raw values per cell (left) and as fold change from baseline conditions per imaging
435 field (right). For **L** and **M,** n=151-158 cells, WT; 133-167 cells, KO; 9-10 imaging fields, 3-4
436 experiments. One-way ANOVA with multiple comparisons for single-cell data, two-tailed paired
437 t-test for the paired-plots.
438
439 **Figure 5: Validation of Salsa6f transgenic iPSC-microglia.** (**A**) Representative green (GCaMP6f),
440 red (tdTomato) and Green/Red channel overlay images of transgenic Salsa6f expressing iPSC-
441 microglia at low (resting Ca^{2+}, top row) and high (Peak SOCE, bottom row) cytosolic Ca^{2+} levels.
442 Bright-field image shown for comparison. Cells were treated with TG to evoke SOCE. Scale bar =

443 5 μm. (**B**) Trace of average change in fluorescence intensity of tdTomato (red) and GCamp6f
444 (green) over time (n=32 cells). (**C**) Ratiometric GCaMP6f/ tdTomato signal (Green/ Red or G/R
445 Ratio) over time calculated from (**B**). (**D**) Immunofluorescence images of P2RY13 and IBA1 in WT
446 or Salsa6f-transgenic iPSC-microglia (left). Right panel shows quantification of P2RY13 and IBA1
447 protein expression (n=4 wells, 2 independent images per well, t-test). (**E**) Phagocytosis of
448 Synaptosomes in WT non-transgenic (open circle) and Salsa6f-expressing (closed circle) iPSC-
449 microglia. Cytochalasin D (grey, 10 μM) used as negative control to inhibit phagocytosis. Live
450 cultures imaged on IncuCyte S3 (n=4 wells; 4 images per well). (**F**) Phagocytic load at 24 hrs for
451 synaptosomes, beta-amyloid, zymosan A, and *S. aureus* (n=4 wells; 4 images per well; one way
452 ANOVA with tukey post-hoc test). (**G**) Microglia cell counts at final day of differentiation (n=3
453 wells, t-test). (**H**) Ca^{2+} response to 2.5 μM ADP in WT vs TREM2 KO Salsa6f-expressing iPSC-
454 microglia (n=41-53 cells). (**I**) Fluorescence intensity of tdTomato (red) and GCaMP6f (green) (left
455 axis) simultaneously measured alongside cell displacement (black) (right axis).
456
457 **Figure 6: Cytosolic Ca^{2+} levels tune microglial motility in TREM2 KO cells.** (**A**) Schematic of
458 traditional SOCE pathway with store-refilling (left) and a "Ca^{2+}–clamp" method of sustaining
459 cytoplasmic Ca^{2+} to "low" and "high" levels with 0.2 and 2mM extracellular Ca^{2+} and using TG to
460 inhibit store-refilling (right). (**B**) Average SOCE traces in WT Salsa6f iPSC-microglia showing
461 cytoplasmic Ca^{2+} 'clamped' at different levels after addition of 0.2 or 2 mM extracellular
462 Ca^{2+}(n=78-110 cells). (**C**) Average change in cytoplasmic Ca^{2+} levels in WT and TREM2 KO microglia
463 over 25 minutes after SOCE activation. (**D**) Comparison of Ca^{2+} levels and microglia motility in WT
464 (top) and TREM2 KO (bottom) microglia. Cytosolic Ca^{2+} levels indicated by instantaneous single-
465 cell G/R Ratio (n=74-158 cells). Mean-speed, displacement and track straightness calculated as
466 before in Figures 3 and 4. Yellow (0.2 mM Ca, TG), green (2 mM Ca, TG). Students t-test **** $p <$
467 0.0001; ** $p = 0.0062$; * $p = 0.432$; ns > 0.9999. (**E**) Correlation of instantaneous Ca^{2+} and
468 instantaneous speed in WT and KO cells. Red line denotes 10 μm/sec (cells above this threshold
469 considered "fast-moving"). For WT: $p < 0.0001$; $r = -0.1316$; number pairs = 5850. For KO: $p <$
470 0.0001; $r = -0.1433$; number pairs = 6063 (Spearman's correlation). (**F**) Mean speed of cells binned
471 by instantaneous G/R Ca^{2+} ratio (1-way ANOVA **** $p < 0.0001$). Each data point is calculated

472 for a bin increment of 0.5 G/R ratio. (**G**) Percentage of fast-moving cells quantified as a function
473 of G/R Ca^{2+} ratio. X-axis G/R ratios binned in increments of 0.5 as in **F**. In **E-G**, n=78-100 cells.
474
475 **Figure 7: Migration deficits in TREM2 KO microglia are rescued by inhibition of purinergic**
476 **signaling.** (**A**) Migration towards ADP in a two-chamber microfluidic device. Representative
477 images of RFP expressing microglia that migrated into the central chamber 3 days after 100
478 ng/mL ADP addition. Dotted circle delineates separation of inner and outer chamber. Scale bar =
479 500 μm. Quantification of microglial migration (right panel). Migrated cell counts are normalized
480 to WT cells treated with ADP (n=3-4 experiments; One-way ANOVA with multiple comparisons).
481 (**B**) Baseline subtracted peak ratiometric Ca^{2+} signal in response to 2.5 μM ADP in 1 mM
482 extracellular Ca^{2+}, and in the presence or absence of 10 μM PSB 0739 (44 cells, WT; 39-43 cells,
483 KO; representative of 3 independent experiments; Students t-test). (**C**) Two-chamber migration
484 to 100 ng/mL ADP with or without 10 μM PSB 0739. Values are normalized to WT cells with ADP
485 (n=3-4 experiments; One-way ANOVA with multiple comparisons). Representative images shown
486 on the left. Scale bar = 500 μm.
487
488 **Figure 8: A Model for Ca^{2+} regulation of ADP-mediated chemotaxis in microglia lacking TREM2.**
489 (**A**) Dose-response curve comparing ADP-mediated peak-Ca^{2+} response in WT and TREM2 KO
490 microglia. EC50 for KO cells is more than 10-fold lower than WT microglia. P2Y12 and 13 receptor
491 expression is higher in cells lacking TREM2 rendering them hypersensitive to ADP signaling. (**B**)
492 Due to exaggerated purinergic ADP signaling, microglia lacking TREM2 exhibit a deficit in moving
493 towards ADP gradients. Despite moving in straighter tracks, TREM2 KO cells migrate in all
494 directions contributing to their chemotactic inefficiency. Partially suppressing P2Y12 receptor
495 signaling would shift the response to ADP to the right (arrow in panel A) and lower cytosolic Ca^{2+}
496 in TREM2 KO cells, restoring their ability to move towards the ADP gradient.
497

498 **Supplementary Figure Legends**

499

500 **Figure 1-figure supplement 1: Differential engagement of SOCE by purinergic agonists.** (**A**) Ca^{2+}
501 responses in TREM2 KO iPSC-microglia 5 min after application of 2.5 μM ADP (blue), 2.5 μM ATP
502 (red), and 10 μM UTP (yellow) that are gated for similar initial peak Ca^{2+} response to the agonists
503 shown in the left panel (n=11-65 cells, pooled from 2 experiments). (**B**) Ratiometric Ca^{2+}
504 responses in WT iPSC-microglia treated with 2-APB (50 μM) or Gd^{3+} (5 μM) to block store-
505 operated Ca^{2+} entry (SOCE) (n= 80-148 cells). P-value calculated for **A** and **B** using ordinary one-
506 way ANOVA with multiple comparisons.

507

508 **Figure 1-figure supplement 2: Expression of STIM1, Orai1, and IP3R2 are not altered in TREM2**
509 **KO iPSC-microglia.** (**A**) Volcano plot of differentially expressed genes from bulk RNA-sequencing
510 of WT and TREM2 KO iPSC-microglia (n=4). Genes for IP3R, STIM, and ORAI are highlighted. (**B**)
511 Raw frequency per kilobase million reads (FPKM) in iPSC-microglia. (**C**) RNA normalized read
512 counts of highly expressed isoforms for (**C**) IP3R2, (**D**) STIM1, and ORAI1. Adjusted p-values from
513 DESeq2. (**E**) Immunofluorescence of Orai1 in WT and TREM2 KO iPSC-microglia. n=3 images per
514 well from 4 independent wells; students t-test.

515

516 **Figure 1-figure supplement 3: SOCE is not altered in TREM2 KO microglia.** (**A**) Representative
517 single-cell trace of Ca^{2+} signal in response to ADP in 1mM extracellular Ca^{2+} buffer showing the
518 scheme for measuring ER store-release as the initial Ca^{2+} peak and SOCE as cytosolic Ca^{2+} level 5
519 min after ADP application. (**B**) Scatter-plot showing correlation of initial ADP-induced Ca^{2+}
520 response (store-release) and cytoplasmic Ca^{2+} after 5 minutes (SOCE) in WT (grey) and KO (green)
521 cells (N= 866-935 cells from multiple imaging runs with a range of ADP doses). (**C**) Correlation
522 between ADP-induced store-release and SOCE using the same data-set in B but with each data-
523 point representing average Ca^{2+} response to the following doses of ADP in 1 mM Ca^{2+} (in μM:
524 0.001, 0.1, 0.5, 1, 2, 2.5, 5, 10). WT and TREM2 KO data are overlaid in the same scatter-plot.
525 (Comparison of slopes between WT and TREM2 KO: p-value = 0.7631; Extra sum of squares F
526 test).

527 **Figure 3-figure supplement 1: ADP-mediated process extension in WT iPSC-microglia. (A)**
528 Representative images of a cell (Cell 1) from a time-lapse experiment showing increased
529 branching and extension of processes in GFP-expressing WT iPSC-microglia, at times indicated
530 following addition of 2.5 μM ADP. Bright field DIC images (top row) and GFP images (bottom row)
531 are shown. (**B**) Another example of a cell (Cell 2) showing process extension in the same imaging
532 field. (**C**) A motile cell (Cell 3) in the same imaging field is shown for comparison. Note the lack of
533 displacement in cells that extend their process, and lack of significant process extension in a
534 highly motile cell. Scale bar: 15 μM.
535
536 **Figure 4-figure supplement 1: Motility analysis in WT and TREM2 KO iPSC-microglia.** (**A**) Scratch
537 Wound performed via IncuCyte S3 WoundMaker shows no difference in migration into the
538 scratch wound area. Two-way ANOVA with multiple comparisons, n=2 images per well over 3
539 independent wells. (**B**) Summary of microglial mean speeds, displacement over 10 min, and track
540 straightness in open-field migration (student's t-test). (**C**) Flower plots show similar displacement
541 from origin for WT (left) and TREM2 KO (right) cells. (**D, E**) Directional Autocorrelation calculated
542 via DiPer excel macro. Due to lack of directional gradient, directional autocorrelation of motility
543 vectors is expected to drop quickly. Time constants for best-fit single exponential curves are
544 indicated, consistent with increased straightness for TREM2 KO cells treated with ADP. (**E**)
545 Directional autocorrelation of WT (grey) and TREM2 KO (green) iPSC-microglia at baseline (open
546 circles) or after ADP addition (filled circles). Mean autocorrelation values in the first 5 minutes
547 (one-way ANOVA) and time (min) until autocorrelation reaches zero.
548
549 **Figure 4-figure supplement 2: Comparison of process extension in WT and TREM2 KO Microglia.**
550 Branching and process extension in WT and TREM2 KO iPSC-microglia 30 min after addition of
551 ADP in 1 mM (**A, B**) or 0 mM extracellular Ca^{2+} buffer (**C, D**). (**A**) Data displayed as paired-plots
552 showing average branch number per cell in an imaging field (top row) and normalized to pre-ADP
553 values for each imaging field (middle row). Bottom row shows fold change in branching after ADP
554 treatment for WT (grey) and KO (green) iPSC-microglia. (**B**) Changes in process length in the same
555 dataset as **A**. n=151-158 cells, WT; 133-167 cells, KO; 9-10 imaging fields, 3-4 experiments. (**C, D**)

556 Same analysis as **A, B** but with ADP in Ca^{2+} free buffer. n=137-143 cells, 8 imaging fields, 2-3
557 experiments. (**A-D**) p-values calculated by two-tailed paired Students t-test for the paired-plots,
558 and by unpaired t-test when comparing fold-change in WT and KO cells.
559
560 **Figure 5-figure supplement 1: Generation of Salsa6f iPSC line.** Construct design for the Salsa6f
561 knock-in template (top) Primers for sequence validation marked with blue arrows. Sanger
562 sequencing to confirm proper integration of Salsa6f cassette into AAVS1 Safe Harbor Locus
563 (bottom).
564
565 **Figure 6-figure supplement 1: Motility analysis with Ca^{2+} "clamp".** (**A**) Ca^{2+} ratios and microglia
566 motility in WT (top) and KO (bottom) microglia. Ca^{2+} clamp experiments with ADP added: yellow
567 (0.2 mM Ca^{2+}, TG + ADP), green (2 mM Ca^{2+}, TG + ADP). Students t-test **** $p < 0.0001$; *** $p =$
568 0.0001. n=164-393 cells. (**B, C**) Ca^{2+} tuning of mean speed and track displacement length in 0.2
569 mM "Ca^{2+} clamp": correlation between instantaneous Ca^{2+} and cumulative displacement. Each
570 dot represents an individual cell for an individual frame. Dotted red line represents displacement
571 of 200 um^2. WT cells (**B**) displace less than KO cells (**C**). For each cell type, larger displacements
572 are correlated with lower G/R Ca^{2+} ratios. Cells which maintain elevated cytoplasmic Ca^{2+} do not
573 displace as far. For WT: $p < 0.0001$; $r = -0.4778$; number pairs = 5973. For KO: $p < 0.0001$; $r = -$
574 0.3699; number pairs = 5761 (Spearman's correlation).
575
576
577

578 **Materials and Methods**

579 **Key Resources Table**

Reagent type (species) or resource	Designation	Source or reference	Identifiers	Additional Information
Cell line (Human)	WT iPSC-microglia	UCI ADRC iPSC Core	ADRC5	iPSC-derived microglial line
Cell line (Human)	TREM2 KO iPSC microglia	Blurton-Jones lab	ADRC5 Clone 28-18	CRISPR-mediated knockout of TREM2 on the WT iPSC line
Cell line (Human)	WT GFP- expressing iPSC-microglia	Coriell	AICS-0036	iPSC-line with GFP tagged to αtubulin. Originally developed by Dr. Bruce Conklin
Cell line (Human)	TREM2 KO GFP-expressing iPSC-microglia	Blurton-Jones lab	GFP Clone 1	CRISPR-mediated knockout of TREM2 on the WT GFP^+ iPSC line
Cell line (Human)	WT RFP-expressing iPSC-microglia	Coriell	AICS-0031-035	iPSC-line with RFP tagged to αtubulin. Originally developed by Dr. Bruce Conklin
Cell line (Human)	TREM2 KO RFP-expressing iPSC-microglia	Blurton-Jones lab	RFP Clone 6	CRISPR-mediated knockout of TREM2 on the WT RFP^+ iPSC line
Cell line (Human)	WT Salsa6f-expressing iPSC-microglia	UCI ADRC iPSC Core	ADRC76 Clone 8	iPSC-line expressing a GCaMP6f-tdTomato fusion construct (Salsa6f)
Cell line (Human)	TREM2 KO Salsa6f-expressing iPSC microglia	Blurton-Jones lab	ADRC76 Clone 8 Clone 98	CRISPR-mediated knockout of TREM2 on the WT $Salsa6f^+$ iPSC line
Plasmid Construct (transgene)	Salsa6f	Addgene	Plasmid# 140188	A genetically encoded Calcium Indicator with tdTomato linked to GCaMP6f by a V5 epitope tag.
Other	DMEM/F12, HEPES, no Phenol red	Thermo Fisher Scientific	11038021	Microglia differentiation cell culture medium
Other	TeSR™-E8™	STEMCELL Technologies	05990	Stem cell culture medium
Other	StemDiff Hematopoietic kit	STEMCELL Technologies	05310	
Peptide/ Recombinant protein	Non-essential amino acids	Gibco	11140035	

Peptide/ Recombinant protein	Glutamax	Gibco	35050061	
Peptide/ Recombinant protein (human)	Insulin	Sigma	I2643	
Peptide/ Recombinant protein	B27	Gibco	17504044	
Peptide/ Recombinant protein	N2	Gibco	A1370701	
Peptide/ Recombinant protein	Insulin-transferrin-selenite	Gibco	41400045	
Peptide/ Recombinant protein (human)	IL-34	Peprotech	200-34	
Peptide/ Recombinant protein (human)	TGFβ1	Peprotech	100-21	
Peptide/ Recombinant protein (human)	M-CSF	Peprotech	300-25	
Peptide/ Recombinant protein	CX3CL1	Peprotech	300-31	
Peptide/ Recombinant protein	CD200	Novoprotein	C311	
Peptide/ Recombinant protein	Fibronectin	STEMCELL Technologies	07159	
Other	Matrigel	Corning	356231	
Other	ReLeSR	STEMCELL Technologies	5872	Human pluripotent stem cell selection and passing reagent
Other	Goat Serum	Thermo Fisher Scientific	10000C	
Other	fluorescent beta-amyloid 1-42 (647)	Anaspec	AS64161	
Other	pHrodo tagged zymosan A beads	Thermo Fisher Scientific	P35364	
Other	pHrodo tagged S. Aureus	Thermo Fisher Scientific	A10010	
Other	Human Stem Cell Nucleofector kit 2	Lonza	VPH-5022	

Other	Alt-R CRISPR-Cas9 tracrRNA	IDTDNA	107253	
Other	Alt-R HiFi Cas9 Nuclease	IDTDNA	1081061	
Antibody	Anti-human P2RY12	Sigma	HPA014518	
Antibody	Anti-human P2RY13	Alomone	APR-017	
Antibody	Anti-human Orai1	Alomone	ALM-025	
Antibody	Anti-human IBA1	Wako	019-19741	
Antibody	Goat anti-rabbit 488	Thermo Fisher Scientific	A11008	Secondary antibody
Antibody	Goat anti-mouse 555	Thermo Fisher Scientific	A21424	Secondary antibody
Antibody	Goat anti-rabbit 555	Thermo Fisher Scientific	A21429	Secondary antibody
Chemical compound, drug	Fluo-4 AM	Thermo Fisher Scientific	F14201	
Chemical compound, drug	Fura-red AM	Thermo Fisher Scientific	F3021	
Chemical compound, drug	Pluronic F-127	Thermo Fisher Scientific	P3000MP	
Chemical compound, drug	Cal-520 AM	AAT Bioquest	21130	
Chemical compound, drug	ci-IP3/PM	SiChem	6210	Caged-inositol triphosphate analog
Chemical compound, drug	Hoeschst	Thermo Fisher Scientific	R37165	
Chemical compound, drug	ADP	Sigma-Aldrich	A2754	
Chemical compound, drug	ATP	Sigma-Aldrich	A9187	
Chemical compound, drug	UTP	Sigma-Aldrich	U1006	
Chemical compound, drug	PSB 0739	Tocris	3983	
Chemical compound, drug	MRS 2211	Tocris	2402	
Chemical compound, drug	2-APB	Sigma-Aldrich	D9754	
Chemical compound, drug	Gadolinium	Sigma-Aldrich	G7532	
Chemical compound, drug	EGTA	Sigma-Aldrich	E8145	
Chemical compound, drug	1-thioglycerol	Sigma-Aldrich	M6145	
Chemical compound, drug	CloneR	STEMCELL Technologies	05888	Defined supplement for single-cell cloning of human iPS cells

Chemical compound, drug	Thiazovivin	STEMCELL Technologies	72252	ROCK inhibitor
Other	35mm glass-bottom dish	MatTek	P35G-1.5-14-C	1.5 coverslip, 14mm glass diameter
Other	Incubation perfusion Lid for 35mm dishes	Tokai Hit	LV200-D35FME	Perfusion lid with inlet and outlet
Other	Laser Scanning Confocal Microscope	Olympus	FV3000	Equipped with Resonant Scanner, IX3-ZDC2 Z-drift compensator, 40x silicone oil objective, 20x air objective
Other	Stage Top Incubation System	Tokai Hit	STXG	Temperature and humidity control for FV3000 microscope stage
Other	Nikon Eclipse T*i* microscope system	Nikon		Equipped with a 40x oil immersion objective (N.A.: 1.3; Nikon) and an Orca Flash 4.0LT CMOS camera (Hamamatsu)
Other	Chemotaxis Assay Chamber	Hansang Cho Lab		
Other	IncuCyte S3 Live-Cell Analysis System	Sartorius		
Other	Essen Incucyte WoundMaker	Sartorius	4493	
Software, algorithm	GraphPad Prism 9.1.0			Data analysis, statistical analysis
Software, algorithm	Fiji (Image J)			Image analysis
Software, algorithm	Incucyte 2020C			Image acquisition and analysis
Software, algorithm	IMARIS 9.7.0			Cell tracking and image analysis
Software, algorithm	Flika			Image analysis
Software, algorithm	DiPer Excel Macros		PMID: 25033209	Data analysis, directional persistence

580

581 **Generation of iPSCs from human fibroblasts:** Human induced pluripotent stem cell lines were

582 generated by the University of California, Irvine Alzheimer's Disease Research Center (UCI ADRC)

583 Induced Pluripotent Stem Cell Core from subject fibroblasts under approved Institutional Review

584 Boards (IRB) and human Stem Cell Research Oversight (hSCRO) committee protocols. Informed
585 consent was received from all participants who donated fibroblasts. Reprogramming was
586 performed with non-integrating sendai virus in order to avoid integration effects. To validate new
587 iPSC lines, cells were karyotyped by G-banding and tested for sterility. Pluripotency was verified
588 by Pluritest Array Analysis and trilineage in vitro differentiation. Additional GFP- and RFP-αtubulin
589 expressing iPSC lines (AICS-0036 and AICS-0031-035) were purchased from Coriell and originally
590 generated by Dr. Bruce Conklin. iPSCs were grown antibiotic free on Matrigel (Corning) in
591 complete mTeSR1 or TeSR-E8 medium (STEMCELL Technologies) in a humidified incubator (5%
592 CO_2, 37° C). All lines will be available upon request to the corresponding author.
593 **CRISPR-mediated knockout of TREM2:** Genome editing was performed as in McQuade et al.
594 2020[39]. Briefly, iPSCs were nucleofected with RNP complex targeting the second exon of TREM2
595 and allowed to recover overnight. Transfected cells were dissociated with pre-warmed Accutase
596 then mechanically plated to 96-well plates for clonal expansion. Genomic DNA from each colony
597 was amplified and sequenced at the cut site. The amplification from promising clones was
598 transformed via TOPO cloning for allelic sequencing. Knockout of TREM2 was validated by
599 western blotting (AF1828, R&D) and HTRF (Cisbio) [39].
600 **iPSC-microglia differentiation:** iPSC-microglia were generated as described in [46]. Briefly, iPSCs
601 were directed down a hematopoetic lineage using the STEMdiff Hematopoesis kit (STEMCELL
602 Technologies). After 10-12 days in culture, CD43+ hematopoteic progenitor cells are transferred
603 into a microglia differentiation medium containing DMEM/F12, 2× insulin-transferrin-selenite, 2×
604 B27, 0.5× N2, 1× Glutamax, 1× non-essential amino acids, 400 µM monothioglycerol, and 5 µg/mL
605 human insulin. Media was added to cultures every other day and supplemented with 100 ng/mL

606 IL-34, 50 ng/mL TGF-β1, and 25 ng/mL M-CSF (Peprotech) for 28 days. In the final 3 days of
607 differentiation 100 ng/mL CD200 (Novoprotein) and 100 ng/mL CX3CL1 (Peprotech) were added
608 to culture.

609 **Confocal Laser Scanning Microscopy:** Unless otherwise stated, cells were imaged on an Olympus
610 FV3000 confocal laser scanning inverted microscope equipped with high-speed resonance
611 scanner, IX3-ZDC2 Z-drift compensator, 40x silicone oil objective (NA 1.25) and a Tokai-HIT stage
612 top incubation chamber (STXG) to maintain cells at 37°C. To visualize Salsa6f, 488 nm and 561
613 nm diode lasers were used for sequential excitation of GCaMP6f (0.3% laser power, 450V channel
614 voltage, 494-544nm detector width) and TdTomato (0.05% laser power, 450V channel voltage,
615 580-680nm detector width), respectively. Fluo-4 and Fura-red were both excited using a 488 nm
616 diode laser (0.07% laser power, 500V channel voltage, 494-544nm detector width for Fluo-4;
617 0.07% laser power, 550V channel voltage, 580-680nm detector for Fura-Red). Two high-
618 sensitivity cooled GaAsP PMTs were used for detection in the green and red channels
619 respectively. GFP was excited using the same settings as GCaMP6f. Other image acquisition
620 parameters unique to Ca^{2+} imaging, microglia process and cell motility analysis are indicated in
621 the respective sections.

622 **Measurement of intracellular Ca^{2+}:**

623 *Cell preparation:* iPSC-microglia were plated on fibronectin-coated (5 µg/mL) glass-bottom 35
624 mm dishes (MatTek, P35G-1.5-14-C) overnight at 60 % confluence. Ratiometric Ca^{2+} imaging was
625 done using Fluo-4 AM and Fura-Red AM dyes as described previously[39]. Briefly, cells were loaded
626 in microglia differentiation medium with 3 µM Fluo-4 AM and 3 µM Fura-Red AM (Molecular
627 Probes) in the presence of Pluronic Acid F-127 (Molecular Probes) for 30 min at room

628 temperature (RT). Cells were washed with medium to remove excess dye and 1 mM Ca^{2+} Ringer's
629 solution was added to the 35 mm dish before being mounted on the microscope for live cell
630 imaging. We note that iPSC-microglia are sensitive to shear forces and produce brief Ca^{2+} signals
631 in response to solution exchange that are dependent on extracellular Ca^{2+}, and that these are
632 more prominent at 37° C. To minimize these confounding effects, cells were imaged at RT and
633 perfusion was performed gently. Salsa6f-expressing iPSC-microglia were prepared for Ca^{2+}
634 imaging in the same way as conventional microglia, but without the dye loading steps. The
635 following buffers were used for Ca^{2+} imaging: (1) 1 or 2 mM Ca^{2+} Ringer solution comprising 155
636 mM NaCl, 4.5 mM KCl, 1 mM $CaCl_2$, 0.5 mM $MgCl_2$, 10 mM glucose, and 10 mM HEPES (pH
637 adjusted to 7.4 with NaOH), (2) Ca^{2+}-free Ringer solution containing: 155 mM NaCl, 4.5 mM KCl,
638 1.5 mM $MgCl_2$, 10 mM glucose, 1 mM EGTA, 10 mM HEPES, pH 7.4. Live cell imaging was
639 performed as described earlier. Cells were treated with ADP as indicated in the results section.
640 *Data acquisition:* Time-lapse images were acquired in a single Z-plane at 512 x 512 pixels (X =
641 318.2 µm and Y = 318.2 µm) and at 2-3 sec time intervals using Olympus FV3000 software. Images
642 were time averaged over 3 frames to generate a rolling average and saved as .OIR files.
643 *Data analysis:* Time-lapse videos were exported to Fiji- ImageJ (https://imagej.net/Fiji),
644 converted to tiff files (16-bit) and background subtracted. Single-cell analysis was performed by
645 drawing ROIs around individual cells in the field and average pixel intensities in the green and red
646 channels were calculated for each ROI at each time-point. GCaMP6f/ TdTomato (G/R Ratio) and
647 Fluo-4/Fura-Red ratio was then obtained to further generate traces showing single-cell and
648 average changes in cytosolic Ca^{2+} over time. Single-cell ratio values was used to calculate Peak
649 Ca^{2+} signal and responses at specific time points after agonist application. Peak Ca^{2+} signal for

650 each cell was baseline subtracted, which was calculated as an average of 10 minimum ratio values
651 before application of agonist.

652 **Microglia process extension analysis:**

653 *Data acquisition:* GFP-expressing iPSC-microglia were plated overnight on 35 mm glass bottom
654 dishes at 40-50% confluence. Cells were imaged by excitation of GFP on the confocal microscope
655 at 37° C as described earlier. To study process extension in response to ADP, two sets of GFP
656 images were obtained for each field of view across multiple dishes: before addition of ADP
657 (baseline) and 30 min after application of ADP. Images were acquired as a Z-stack using the Galvo
658 scanner at Nyquist sampling. Adjacent fields of view were combined using the Stitching function
659 of the Olympus FV3000 Software and saved as .OIR files.

660 *Process Analysis:* The basic workflow for microglia process analysis was adapted from Morrison
661 et al, Sci. Rep, 2017 [66]. Image stacks (.OIR files) were exported to Fiji- Image J and converted into
662 16-bit Tiff files using the Olympus Viewer Plugin (https://imagej.net/OlympusImageJPlugin).
663 Maximum intensity projection (MIP) image from each Z-stack was used for further processing
664 and analysis. MIP images were converted to 8-bit grey scale images, to which a threshold was
665 applied to obtain 8-bit binary images. The same threshold was used for all sets of images, both
666 before and after ADP application. Noise reduction was performed on the binary images using the
667 Process -> Noise -> Unspeckle function. Outlier pixels were eliminated using Process -> Noise ->
668 Outliers function. The binary images were then skeletonized using the Skeletonize2D/3D Plugin
669 for Image J (https://imagej.net/plugins/skeletonize3d). Sparingly, manual segmentation was
670 used to separate a single skeleton that was part of two cells touching each other. The Analyze
671 Skeleton Plugin (https://imagej.net/plugins/analyze-skeleton/) was then applied to the

672 skeletonized images to obtain parameters related to process length and number of branches for
673 each cell in the imaging field. Processes were considered to be skeletons > 8 µm. The data was
674 summarized as average process length and number of branches, before and after ADP application
675 for a specific imaging field, normalized to the number of cells in the field which allowed for
676 pairwise comparison. Additionally, single cell data across all experiments were also compared in
677 some instances.

678 **IP_3 uncaging:** Whole-field uncaging of i-IP_3, a poorly metabolized IP_3 analog, was performed as
679 previously described [67] with minor modifications. Briefly, iPSC-microglia were loaded for 20 min
680 at 37° C with either Cal520 AM or Cal590 AM (5 µM, AAT Bioquest), and the cell permeable, caged
681 i-IP_3 analog ci-IP_3/PM (1 µM, SiChem) plus 0.1% Pluronic F-127 in Microglia Basal Medium. Cells
682 were washed and incubated in the dark for further 30 min in a HEPES-buffered salt solution
683 (HBSS) whose composition was (in mM): 135 NaCl, 5.4 KCl, 1.0 MgCl2, 10 HEPES, 10 glucose, 2.0
684 $CaCl_2$, and pH 7.4. Intracellular Ca^{2+} ($[Ca^{2+}]_i$) changes were imaged by employing a Nikon Eclipse
685 T*i* microscope system (Nikon) equipped with a 40x oil immersion objective (N.A.: 1.3; Nikon) and
686 an Orca Flash 4.0LT CMOS camera (Hamamatsu). Cal520 or Cal590 were excited by a 488 or a 560
687 nm laser light source (Vortran Laser Technologies), respectively. i-IP3 uncaging was achieved by
688 uniformly exposing the imaged cells to a single flash of ultraviolet (UV) light (350-400 nm) from
689 a Xenon arc lamp. UV flash duration, and thus the amount of released i-IP_3, was set by an
690 electronically controlled shutter.

691 Image acquisition was performed by using Nikon NIS (Nikon) software. After conversion
692 to stack tiff files, image sequences were analyzed with Flika, a custom-written Python-based
693 imaging analysis software (https://flika-org.github.io/; [68]). After background subtraction, either

694 Cal520 and Cal590 fluorescence changes of each cell were expressed as $\Delta F/F_0$, where F_0 is the
695 basal fluorescence intensity and ΔF the relative fluorescence change ($F_x - F_0$). Data are reported
696 as superplots [69] of at least three independent replicates. Experiments were reproduced with two
697 independent lines. Comparisons were performed by unpaired non-parametric t-test.
698 **Immunocytochemistry:** Cells were fixed with 4 % paraformaldehyde for 7 min and washed 3x
699 with 1X DPBS. For P2RY12 staining, plates were pre-treated with citrate buffer (pH 6.0) for 20 min
700 95° C. Blocking was performed at room temp for 1 hr in 5 % Goat Serum, 0.1 % Triton X-100.
701 Primary antibodies were added at 1:200 overnight 4° C (P2RY12; HPA014518 Sigma) (P2RY13;
702 APR-017, Alomone). Plates were washed 3x before addition of secondary antibodies (Goat anti-
703 Rabbit 488/555, Thermo Fisher Scientific) and Hoeschst (Thermo Fisher Scientific). Images were
704 captured on an Olympus FV3000RS confocal microscope with identical laser and detection
705 settings. Images were analyzed with IMARIS 9.7.0 software.
706 **Scratch wound assay:** Nondirectional motility was analyzed using Essen Incucyte WoundMaker.
707 iPSC-microglia were plated on fibronectin (STEMCELL Technologies) at 90% confluence. Scratches
708 were repeated 4x to remove all cells from the wound area. Scratch wound confluency was imaged
709 every hour until scratch wound was closed (15 hrs). Confluence of cells within the original wound
710 ROI was calculated using IncuCyte 2020C software.
711 **IMARIS Cell Tracking:** For motility assays, iPSC-microglia were tracked using IMARIS 9.7.0
712 software. For videos of GFP lines, cells were tracked using spot identification. For videos of
713 Salsa6f lines, surface tracking was used to determine ratiometric Ca^{2+} fluorescence and motility
714 per cell. In both conditions, tracks were defined by Brownian motion with the maximum distance
715 jump of 4 microns and 10 frame disturbance with no gap filling. Tracks shorter than 3 minutes in

716 length were eliminated from analysis. After automated track formation, tracks underwent
717 manual quality control to eliminate extraneous tracks, merge falsely distinct tracks, and add
718 missed tracks. After export, data was plotted in Prism 9.1.0 or analyzed in excel using DiPer
719 macros for Plot_At_Origin and mean squared distance [57].

720 **Generation of Salsa6f-expressing iPSC lines:** iPSCs were collected following Accutase enzymatic
721 digestion for 3 min at 37° C. 20,000 cells were resuspended in 100 µL nucleofection buffer from
722 Human Stem Cell Nucleofector™ Kit 2 (Lonza). Salsa6f-AAVS1 SHL plasmid Template (2 µg; Vector
723 Builder) and RNP complex formed by incubating Alt-R® S.p. HiFi Cas9 Nuclease V3 (50 µg; IDTDNA)
724 was fused with crRNA:tracrRNA (IDTDNA) duplex for 15 min at 23° C. This complex was combined
725 with the cellular suspension and nucleofected using the Amaxa Nucleofector program B-016. To
726 recover, cells were plated in TeSR™-E8™ (STEMCELL Technologies) media with 0.25 µM
727 Thiazovivin (STEMCELL Technologies) and CloneR™ (STEMCELL Technologies) overnight. The
728 following day, cells were mechanically replated to 96-well plates in TeSR™-E8™ media with 0.25
729 µM Thiazovivin and CloneR™ supplement for clonal isolation and expansion. Plates were
730 screened visually with a fluorescence microscope to identify TdTomato^{+} clones. Genomic DNA
731 was extracted from positive clones using Extracta DNA prep for PCR (Quantabio) and amplified
732 using Taq PCR Master Mix (Thermo Fisher Scientific) to confirm diallelic integration of the Salsa6f
733 cassette. A clone confirmed with diallelic Salsa6f integration in the AAVS1 SHL was then
734 retargeted as previously described[39] to knock-out Trem2.

735 **Phagocytosis assay:** Phagocytosis of transgenic iPSC-microglia was validated using IncuCyte S3
736 Live-Cell Analysis System (Sartorius) as in McQuade et al. 2020[39]. Microglia were plated at 50%
737 confluency 24 hours before substrates were added. Cells were treated with 50 µg/mL pHrodo

738 tagged human AD synaptosomes (isolated as described in McQuade et al. 2020), 100 ng/mL
739 pHrodo tagged zymosan A beads (Thermo Fisher Scientific), 100 ng/mL pHrodo tagged S. Aureus
740 (Thermo Fisher Scientific), or 2 µg/mL fluorescent beta-amyloid (Anaspec). Image masks for
741 fluorescence area and phase were generated using IncuCyte 2020C software.
742 **Chemotaxis assay:** iPSC-microglia were loaded into the angular chamber (2-5K cells/device) to
743 test activation and chemotaxis towards the central chamber containing either ADP (100 ng/mL)
744 or vehicle. When noted, PSB 0739 (10 µM) was added to both the central and angular chamber
745 to inhibit P2RY12. To characterize motility, we monitored the number of recruited microglia in
746 the central chamber for 4 days under the fully automated Nikon TiE microscope (10×
747 magnification; Micro Device Instruments, Avon, MA, USA).
748
749 **Acknowledgments**
750 The authors would like to thank Dr. Andy Yeromin for the development of Excel macros to analyze
751 IMARIS cell tracking. The authors would also like to thank Morgan Coburn for sharing python
752 scripts that aided in the organization of IMARIS output files. This work was supported by T32
753 NS082174 and ARCS foundation (A.M.); NIH R01 NS14609 and AI121945 (M.D.C.); NRF
754 2020R1A2C2010285, 2020M3C7A1023941, and NIH AG059236-01A1 (H.C.); NIH AG048099,
755 AG056303, and AG055524 (M.B.J.); RF1DA048813 (M.B.J. and S.G.); UCI Sue & Bill Gross Stem
756 Cell Research Center Seed Grant (S.G.); and a generous gift from the Susan Scott Foundation
757 (M.B.J.). iPSC lines were generated by the UCI-ADRC iPS cell core funded by NIH AG066519.
758 Experiments using the GFP-expressing iPSC line AICS-0036 were made possible through the Allen
759 Cell Collection, available from Coriell Institute for Medical Research.

760

761 **Declaration of interest:** M.B.J. is a co-inventor of patent application WO/2018/160496, related
762 to the differentiation of pluripotent stem cells into microglia. M.B.J and S.P.G. are co-founders of
763 NovoGlia Inc.

764 **Ethics:** Human iPSC lines were generated by the University of California Alzheimer's Disease
765 Research Center (UCI ADRC) stem cell core. Subject fibroblasts were collected under approved
766 Institutional Review Boards (IRB) and human Stem Cell Research Oversight (hSCRO) committee
767 protocols. Informed consent was received for all participants.

768 **Data Availability:** RNA sequencing data referenced in Figure 1- figure supplement 2 is available
769 through Gene Expression Omnibus: GSE157652.

770

771

772

References

1. Andersen, M. S. *et al.* Heritability Enrichment Implicates Microglia in Parkinson's Disease Pathogenesis. *Annals of Neurology* **89**, 942–951 (2021).
2. Crotti, A. *et al.* Mutant Huntingtin promotes autonomous microglia activation via myeloid lineage-determining factors. *Nat Neurosci* **17**, 513–521 (2014).
3. Fahira, A., Li, Z., Liu, N. & Shi, Y. Prediction of causal genes and gene expression analysis of attention-deficit hyperactivity disorder in the different brain region, a comprehensive integrative analysis of ADHD. *Behav Brain Res* **364**, 183–192 (2019).
4. Jansen, I. E. *et al.* Genome-wide meta-analysis identifies new loci and functional pathways influencing Alzheimer's disease risk. *Nat. Genet.* (2019) doi:10.1038/s41588-018-0311-9.
5. McQuade, A. & Blurton-Jones, M. Microglia in Alzheimer's disease: Exploring how genetics and phenotype influence risk. *J Mol Biol* **431**, 1805–1817 (2019).
6. Pimenova, A. A. *et al.* Alzheimer's-associated PU.1 expression levels regulate microglial inflammatory response. *Neurobiol Dis* 105217 (2020) doi:10.1016/j.nbd.2020.105217.
7. Tan, L. *et al.* Association of GWAS-linked loci with late-onset Alzheimer's disease in a northern Han Chinese population. *Alzheimers Dement* **9**, 546–553 (2013).
8. Davalos, D. *et al.* ATP mediates rapid microglial response to local brain injury in vivo. *Nat. Neurosci.* **8**, 752–758 (2005).
9. De Simone, R. *et al.* TGF-β and LPS modulate ADP-induced migration of microglial cells through P2Y1 and P2Y12 receptor expression. *J. Neurochem.* **115**, 450–459 (2010).
10. Honda, S. *et al.* Extracellular ATP or ADP Induce Chemotaxis of Cultured Microglia through Gi/o-Coupled P2Y Receptors. *J. Neurosci.* **21**, 1975–1982 (2001).

11. Koizumi, S. *et al.* UDP acting at P2Y6 receptors is a mediator of microglial phagocytosis. *Nature* **446**, 1091–1095 (2007).

12. Dissing-Olesen, L. *et al.* Activation of neuronal NMDA receptors triggers transient ATP-mediated microglial process outgrowth. *J Neurosci* **34**, 10511–10527 (2014).

13. Madry, C. & Attwell, D. Receptors, ion channels, and signaling mechanisms underlying microglial dynamics. *J Biol Chem* **290**, 12443–12450 (2015).

14. Zhang, Y. *et al.* An RNA-Sequencing Transcriptome and Splicing Database of Glia, Neurons, and Vascular Cells of the Cerebral Cortex. *J. Neurosci.* **34**, 11929–11947 (2014).

15. Prakriya, M. & Lewis, R. S. Store-Operated Calcium Channels. *Physiol Rev* **95**, 1383–1436 (2015).

16. McLarnon, J. G. Microglial Store-operated Calcium Signaling in Health and in Alzheimer's Disease. *Curr Alzheimer Res* **17**, 1057–1064 (2020).

17. Mizuma, A. *et al.* Microglial Calcium Release-Activated Calcium Channel Inhibition Improves Outcome from Experimental Traumatic Brain Injury and Microglia-Induced Neuronal Death. *J Neurotrauma* **36**, 996–1007 (2019).

18. Gilbert, D. F. *et al.* Store-Operated Ca2+ Entry (SOCE) and Purinergic Receptor-Mediated Ca2+ Homeostasis in Murine bv2 Microglia Cells: Early Cellular Responses to ATP-Mediated Microglia Activation. *Front Mol Neurosci* **9**, 111 (2016).

19. Hasselmann, J. *et al.* Development of a Chimeric Model to Study and Manipulate Human Microglia In Vivo. *Neuron* (2019) doi:10.1016/j.neuron.2019.07.002.

20. Keren-Shaul, H. *et al.* A Unique Microglia Type Associated with Restricting Development of Alzheimer's Disease. *Cell* **0**, (2017).

21. Krasemann, S. *et al.* The TREM2-APOE Pathway Drives the Transcriptional Phenotype of Dysfunctional Microglia in Neurodegenerative Diseases. *Immunity* **47**, 566-581.e9 (2017).
22. Olah, M. *et al.* Single cell RNA sequencing of human microglia uncovers a subset associated with Alzheimer's disease. *Nature Communications* **11**, 6129 (2020).
23. Sala Frigerio, C. *et al.* The Major Risk Factors for Alzheimer's Disease: Age, Sex, and Genes Modulate the Microglia Response to Aβ Plaques. *Cell Rep* **27**, 1293-1306.e6 (2019).
24. Weisman, G. A., Woods, L. T., Erb, L. & Seye, C. I. P2Y receptors in the mammalian nervous system: pharmacology, ligands and therapeutic potential. *CNS Neurol Disord Drug Targets* **11**, 722–738 (2012).
25. Cserép, C. *et al.* Microglia monitor and protect neuronal function through specialized somatic purinergic junctions. *Science* **367**, 528–537 (2020).
26. Haynes, S. E. *et al.* The P2Y12 receptor regulates microglial activation by extracellular nucleotides. *Nat Neurosci* **9**, 1512–1519 (2006).
27. Suzuki, T. *et al.* Extracellular ADP augments microglial inflammasome and NF-κB activation via the P2Y12 receptor. *European Journal of Immunology* **50**, 205–219 (2020).
28. Wu, Y. *et al.* Aberrant expression of long noncoding RNAs in the serum and myocardium of spontaneous hypertensive rats. *Mol Biol Rep* **46**, 6399–6404 (2019).
29. Eyo, U. B. *et al.* Neuronal hyperactivity recruits microglial processes via neuronal NMDA receptors and microglial P2Y12 receptors after status epilepticus. *J Neurosci* **34**, 10528–10540 (2014).
30. Lou, N. *et al.* Purinergic receptor P2RY12-dependent microglial closure of the injured blood–brain barrier. *PNAS* **113**, 1074–1079 (2016).

31. Leissring, M. A. *et al.* Capacitative calcium entry deficits and elevated luminal calcium content in mutant presenilin-1 knockin mice. *J Cell Biol* **149**, 793–798 (2000).
32. Brawek, B. *et al.* Impairment of in vivo calcium signaling in amyloid plaque-associated microglia. *Acta Neuropathol* **127**, 495–505 (2014).
33. Demuro, A., Parker, I. & Stutzmann, G. E. Calcium Signaling and Amyloid Toxicity in Alzheimer Disease. *J Biol Chem* **285**, 12463–12468 (2010).
34. Mustaly, S., Littlefield, A. & Stutzmann, G. E. Calcium Signaling Deficits in Glia and Autophagic Pathways Contributing to Neurodegenerative Disease. *Antioxid. Redox Signal.* (2018) doi:10.1089/ars.2017.7266.
35. Eichhoff, G., Brawek, B. & Garaschuk, O. Microglial calcium signal acts as a rapid sensor of single neuron damage in vivo. *Biochim Biophys Acta* **1813**, 1014–1024 (2011).
36. Irino, Y., Nakamura, Y., Inoue, K., Kohsaka, S. & Ohsawa, K. Akt activation is involved in P2Y12 receptor-mediated chemotaxis of microglia. *J Neurosci Res* **86**, 1511–1519 (2008).
37. Milior, G. *et al.* Distinct P2Y Receptors Mediate Extension and Retraction of Microglial Processes in Epileptic and Peritumoral Human Tissue. *J Neurosci* **40**, 1373–1388 (2020).
38. Cheng-Hathaway, P. J. *et al.* The Trem2 R47H variant confers loss-of-function-like phenotypes in Alzheimer's disease. *Mol Neurodegener* **13**, 29 (2018).
39. McQuade, A. *et al.* Gene expression and functional deficits underlie TREM2-knockout microglia responses in human models of Alzheimer's disease. *Nature Communications* **11**, 5370 (2020).
40. Ulrich, J. D. *et al.* Altered microglial response to Aβ plaques in APPPS1-21 mice heterozygous for TREM2. *Mol Neurodegener* **9**, 20 (2014).

41. Andrews, S. J., Fulton-Howard, B. & Goate, A. Interpretation of risk loci from genome-wide association studies of Alzheimer's disease. *Lancet Neurol* (2020) doi:10.1016/S1474-4422(19)30435-1.

42. Karch, C. M. *et al.* Expression of Novel Alzheimer's Disease Risk Genes in Control and Alzheimer's Disease Brains. *PLOS ONE* **7**, e50976 (2012).

43. Cheng, Q. *et al.* TREM2-activating antibodies abrogate the negative pleiotropic effects of the Alzheimer's disease variant Trem2R47H on murine myeloid cell function. *J. Biol. Chem.* **293**, 12620–12633 (2018).

44. Gratuze, M. *et al.* Impact of TREM2^{R47H} variant on tau pathology–induced gliosis and neurodegeneration. *J Clin Invest* **130**, 4954–4968 (2020).

45. Abud, E. M. *et al.* iPSC-Derived Human Microglia-like Cells to Study Neurological Diseases. *Neuron* **94**, 278-293.e9 (2017).

46. McQuade, A. *et al.* Development and validation of a simplified method to generate human microglia from pluripotent stem cells. *Molecular Neurodegeneration* **13**, 67 (2018).

47. Andreone, B. J. *et al.* Alzheimer's-associated PLCγ2 is a signaling node required for both TREM2 function and the inflammatory response in human microglia. *Nature Neuroscience* 1–12 (2020) doi:10.1038/s41593-020-0650-6.

48. Cosker, K. *et al.* Microglial signalling pathway deficits associated with the patient derived R47H TREM2 variants linked to AD indicate inability to activate inflammasome. *Sci Rep* **11**, 13316 (2021).

49. Konttinen, H. *et al.* PSEN1ΔE9, APPswe, and APOE4 Confer Disparate Phenotypes in Human iPSC-Derived Microglia. *Stem Cell Reports* (2019) doi:10.1016/j.stemcr.2019.08.004.

50. Piers, T. M. *et al.* A locked immunometabolic switch underlies TREM2 R47H loss of function in human iPSC-derived microglia. *FASEB J.* (2019) doi:10.1096/fj.201902447R.

51. Reich, M. *et al.* Alzheimer's Risk Gene TREM2 Determines Functional Properties of New Type of Human iPSC-Derived Microglia. *Front. Immunol.* **11**, (2021).

52. Dong, T. X. *et al.* T-cell calcium dynamics visualized in a ratiometric tdTomato-GCaMP6f transgenic reporter mouse. *eLife* **6**, e32417 (2017).

53. Michaelis, M., Nieswandt, B., Stegner, D., Eilers, J. & Kraft, R. STIM1, STIM2, and Orai1 regulate store-operated calcium entry and purinergic activation of microglia. *Glia* **63**, 652–663 (2015).

54. Visentin, S., Nuccio, C. D. & Bellenchi, G. C. Different patterns of Ca^{2+} signals are induced by low compared to high concentrations of P2Y agonists in microglia. *Purinergic Signal* **2**, 605–617 (2006).

55. Borges, P. A. *et al.* Adenosine Diphosphate Improves Wound Healing in Diabetic Mice Through P2Y12 Receptor Activation. *Front. Immunol.* **12**, (2021).

56. Hall-Roberts, H. *et al.* TREM2 Alzheimer's variant R47H causes similar transcriptional dysregulation to knockout, yet only subtle functional phenotypes in human iPSC-derived macrophages. *Alzheimers Res Ther* **12**, 151 (2020).

57. Gorelik, R. & Gautreau, A. Quantitative and unbiased analysis of directional persistence in cell migration. *Nature Protocols* **9**, 1931–1943 (2014).

58. Das, R. & Chinnathambi, S. Actin-mediated Microglial Chemotaxis via G-Protein Coupled Purinergic Receptor in Alzheimer's Disease. *Neuroscience* **448**, 325–336 (2020).

59. Negulescu, P. A., Krasieva, T. B., Khan, A., Kerschbaum, H. H. & Cahalan, M. D. Polarity of T cell shape, motility, and sensitivity to antigen. *Immunity* **4**, 421–430 (1996).

60. Park, J. *et al.* A 3D human triculture system modeling neurodegeneration and neuroinflammation in Alzheimer's disease. *Nat. Neurosci.* **21**, 941–951 (2018).
61. Meilandt, W. J. *et al.* Trem2 deletion reduces late-stage amyloid plaque accumulation, elevates the Aβ42:Aβ40 ratio, and exacerbates axonal dystrophy and dendritic spine loss in the PS2APP Alzheimer's mouse model. *J. Neurosci.* (2020) doi:10.1523/JNEUROSCI.1871-19.2019.
62. Lim, H. M. *et al.* UDP-Induced Phagocytosis and ATP-Stimulated Chemotactic Migration Are Impaired in STIM1-/- Microglia In Vitro and In Vivo. *Mediators Inflamm* **2017**, 8158514 (2017).
63. S, P. *et al.* Loss of TREM2 Function Increases Amyloid Seeding but Reduces Plaque-Associated ApoE. *Nature neuroscience* vol. 22 https://pubmed.ncbi.nlm.nih.gov/30617257/?from_single_result=30617257&expanded_search_query=30617257 (2019).
64. Alector Inc. *A Phase 2 Randomized, Double-Blind, Placebo-Controlled, Multicenter Study to Evaluate the Efficacy and Safety of AL002 in Participants With Early Alzheimer's Disease*. https://clinicaltrials.gov/ct2/show/NCT04592874 (2021).
65. Wang, S. *et al.* Anti-human TREM2 induces microglia proliferation and reduces pathology in an Alzheimer's disease model. *J Exp Med* **217**, (2020).
66. Morrison, H., Young, K., Qureshi, M., Rowe, R. K. & Lifshitz, J. Quantitative microglia analyses reveal diverse morphologic responses in the rat cortex after diffuse brain injury. *Sci Rep* **7**, 13211 (2017).

67. Lock, J. T., Parker, I. & Smith, I. F. Communication of Ca(2+) signals via tunneling membrane nanotubes is mediated by transmission of inositol trisphosphate through gap junctions. *Cell Calcium* **60**, 266–272 (2016).

68. Ellefsen, K. L., Settle, B., Parker, I. & Smith, I. F. An algorithm for automated detection, localization and measurement of local calcium signals from camera-based imaging. *Cell Calcium* **56**, 147–156 (2014).

69. Lord, S. J., Velle, K. B., Mullins, R. D. & Fritz-Laylin, L. K. SuperPlots: Communicating reproducibility and variability in cell biology. *J Cell Biol* **219**, (2020).

Figure 1: Microglia lacking TREM2 show exaggerated Ca^{2+} responses to purinergic stimulation.

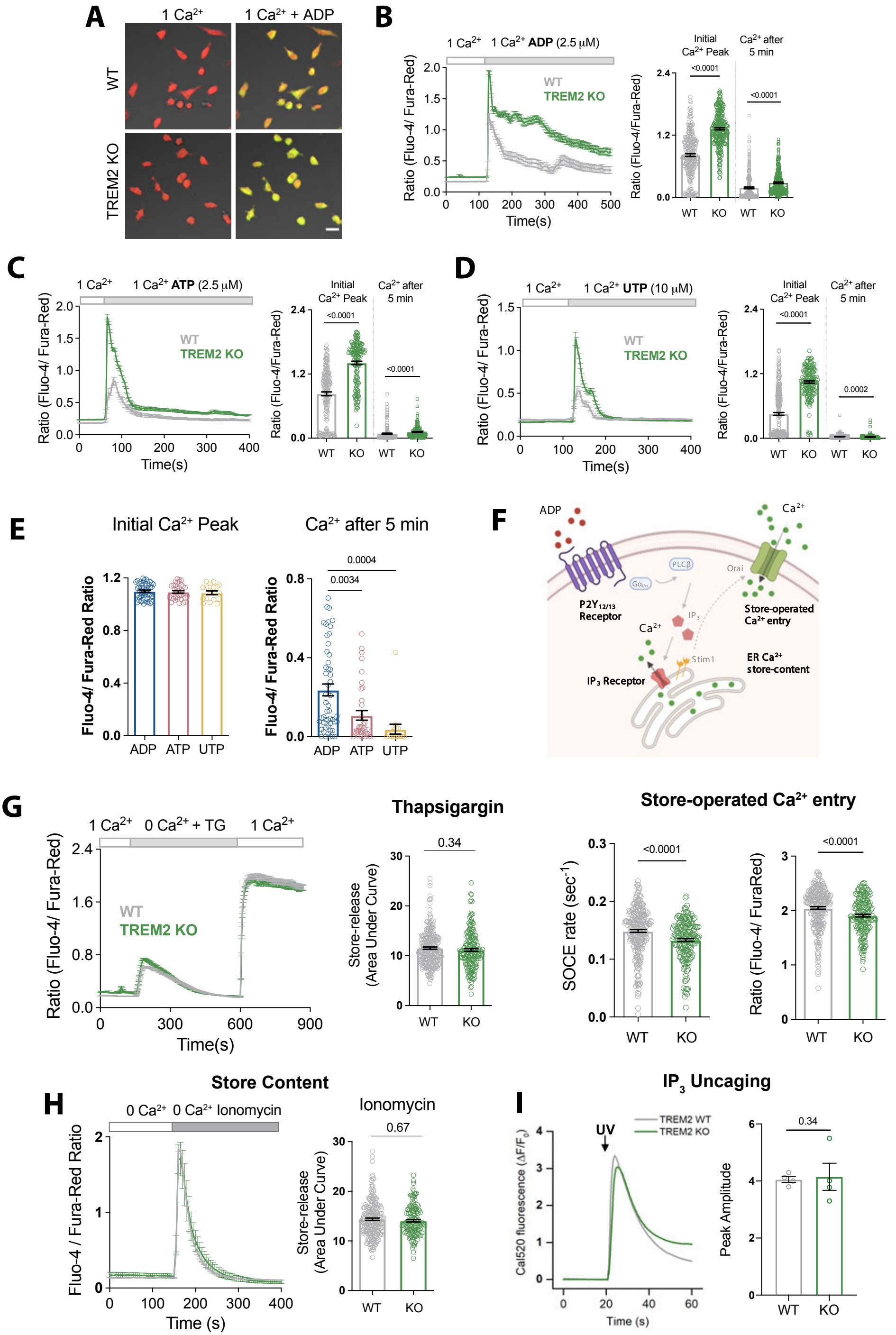

Figure 1-figure supplement 1: Differential engagement of SOCE by purinergic agonists.

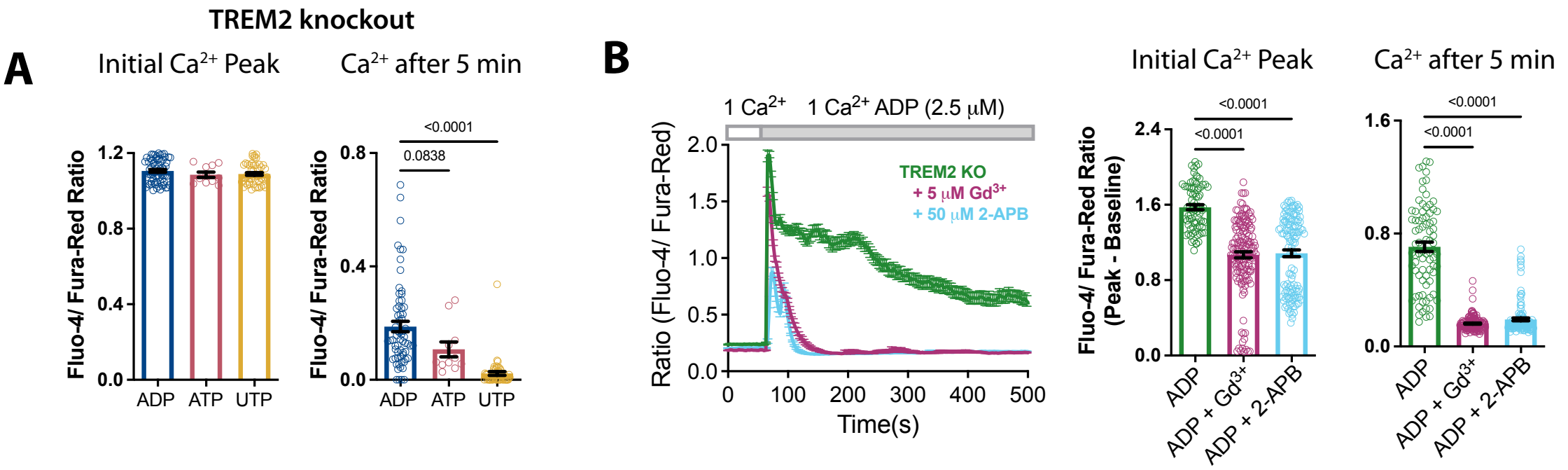

Figure 1-figure supplement 2: Expression of STIM1, Orai1, and IP3R are not altered in TREM2 KO iPSC-microglia.

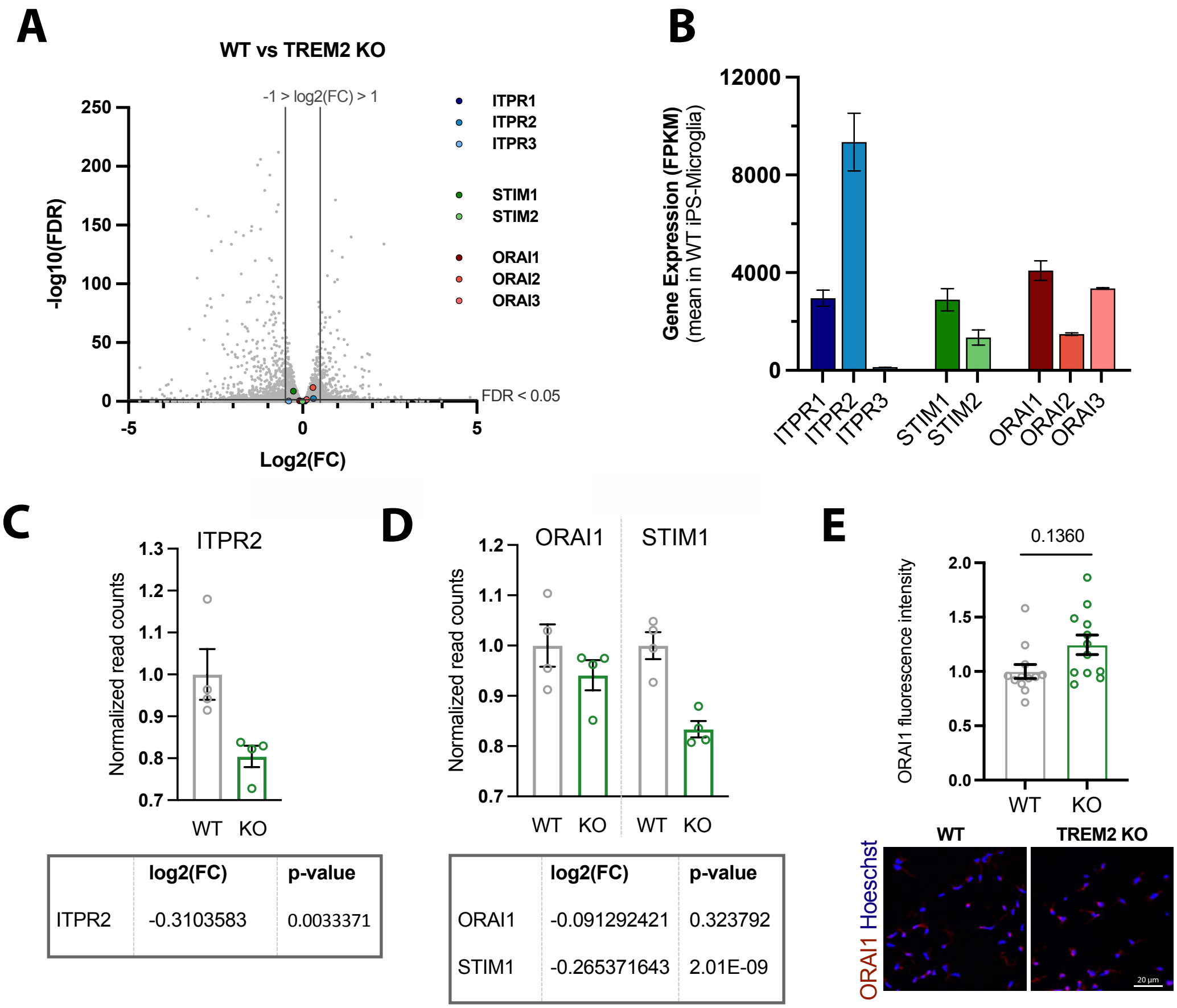

	log2(FC)	p-value
ITPR2	-0.3103583	0.0033371

	log2(FC)	p-value
ORAI1	-0.091292421	0.323792
STIM1	-0.265371643	2.01E-09

Figure 1-figure supplement 3: SOCE engagement is not altered in TREM2 KO.

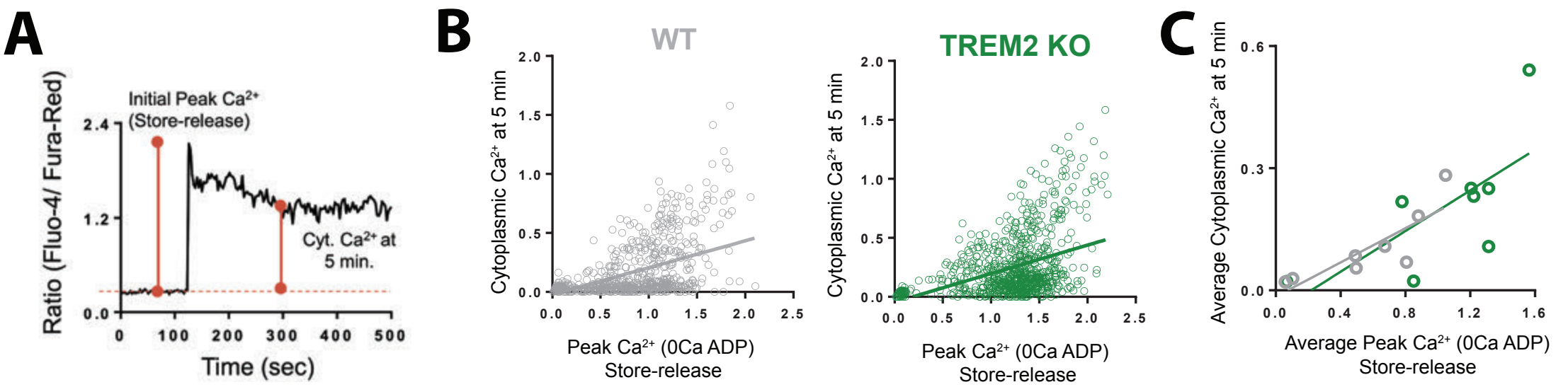

Figure 2: Higher sensitivity of TREM2 KO microglia to ADP is driven by increased purinergic receptor expression

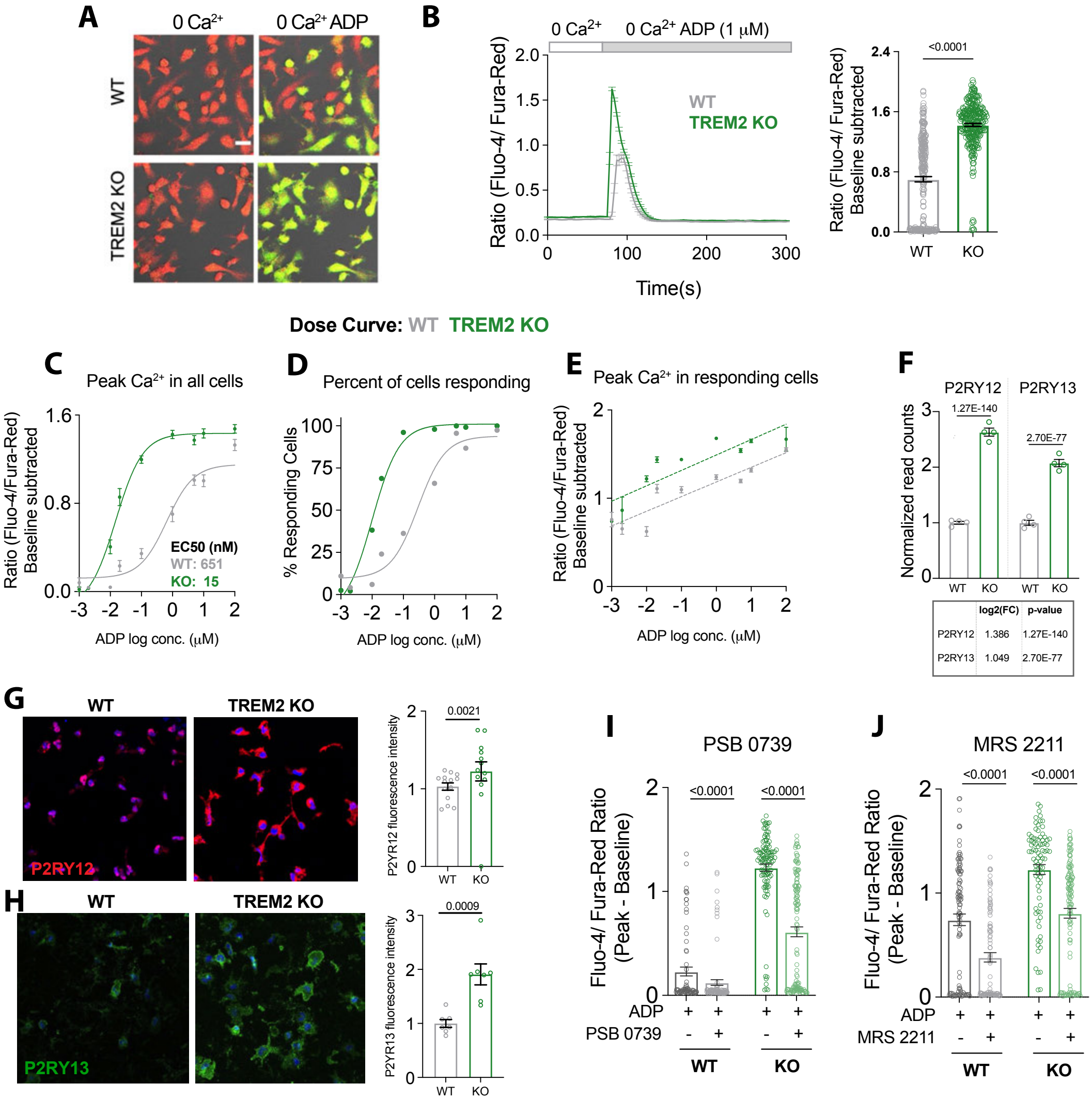

Figure 3: Nondirectional ADP exposure increases WT microglial speed and process extension.

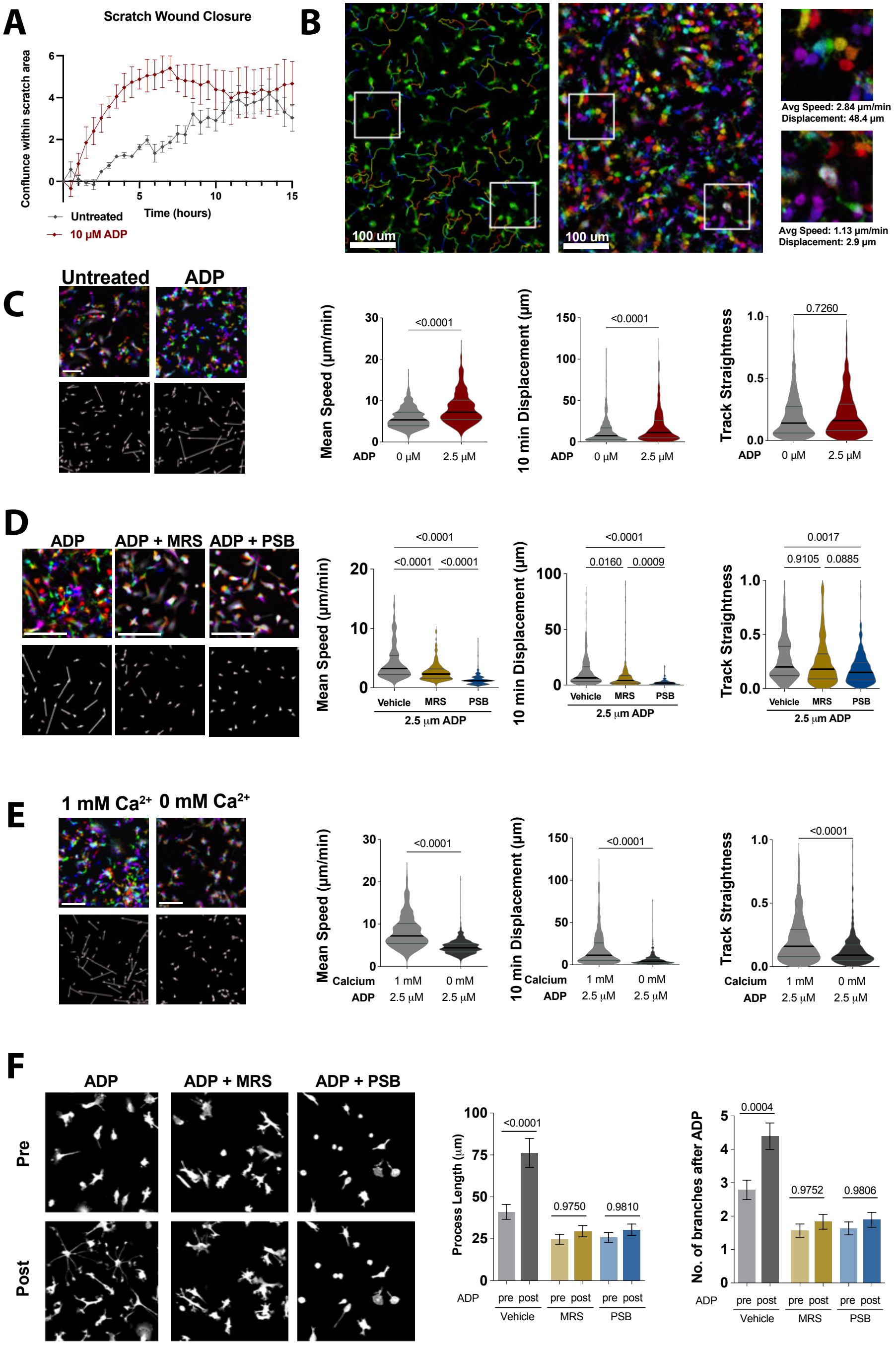

Figure 3-figure supplement 1: ADP-mediated process extension in WT iPSC-microglia.

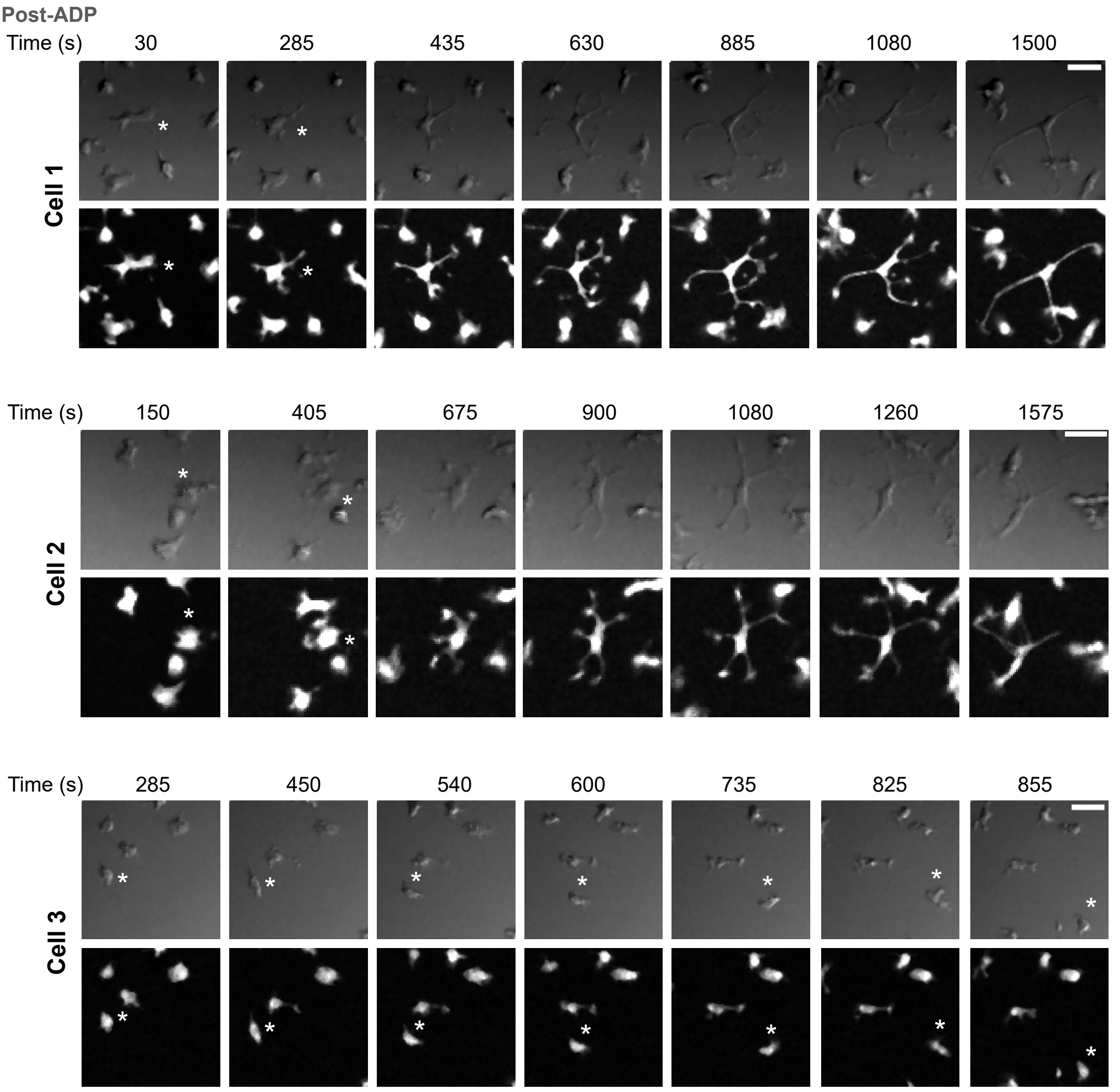

Figure 4: ADP-driven process extension and cell displacement are increased in TREM2 KO iPSC-microglia.

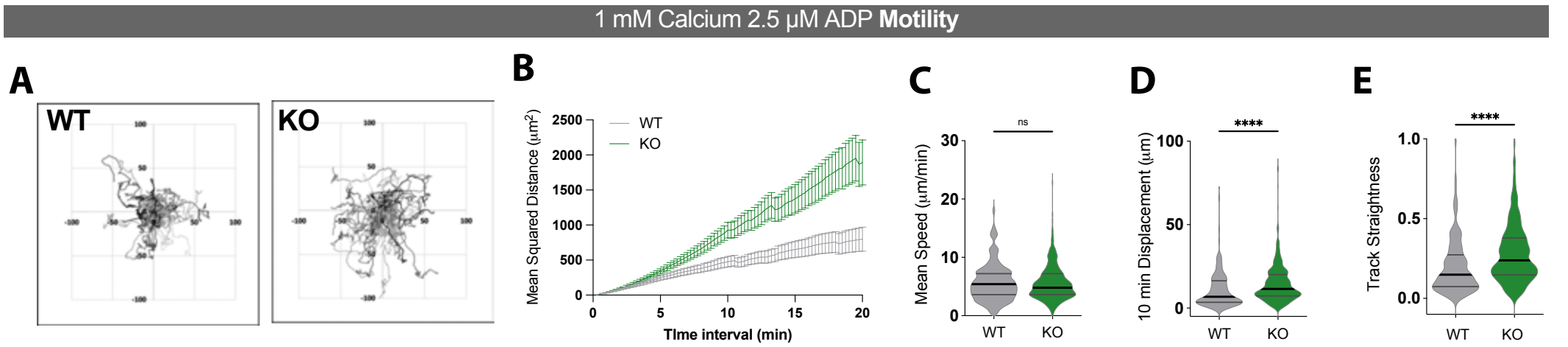

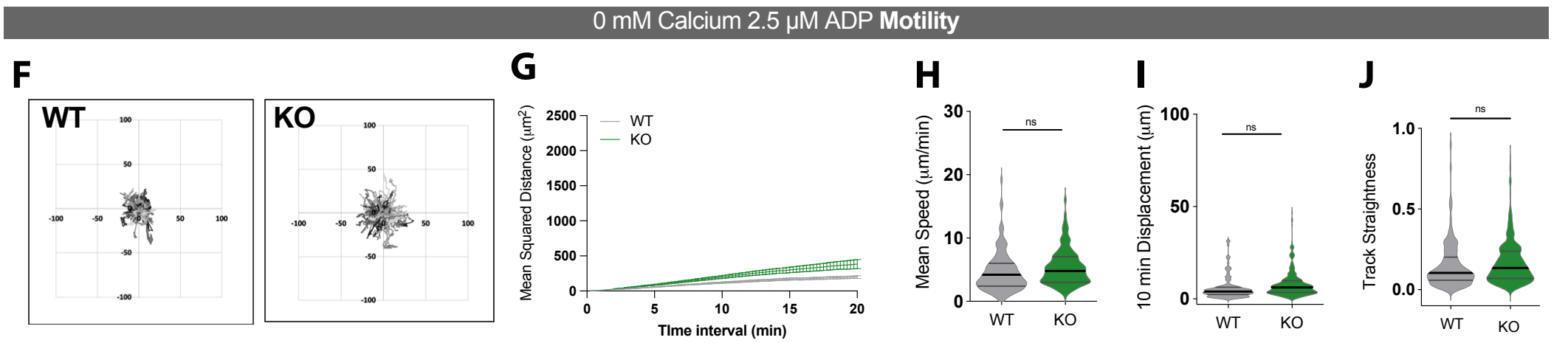

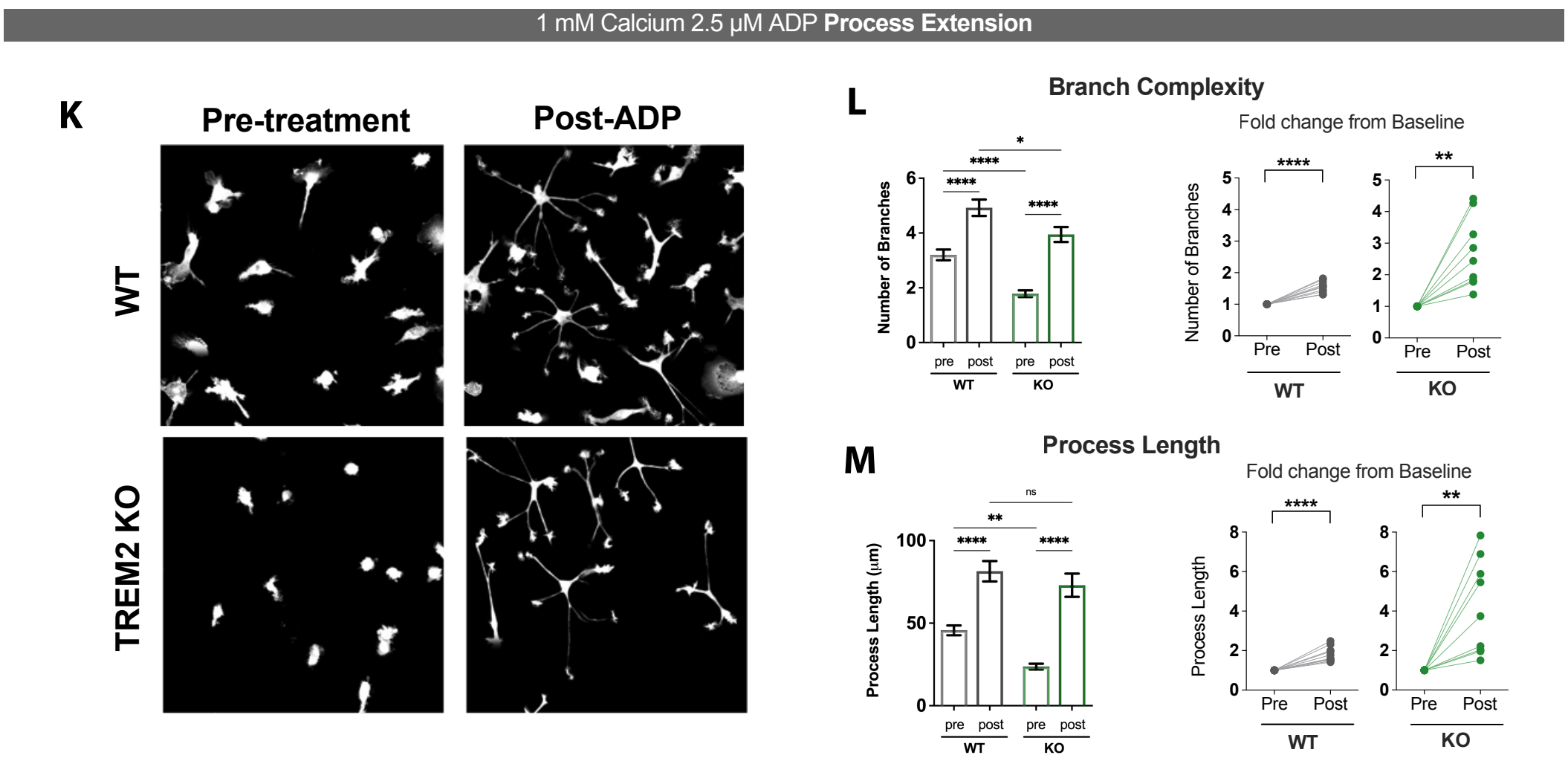

Figure 4-figure supplement 1: Motility analysis in WT and TREM2 KO iPSC-microglia.

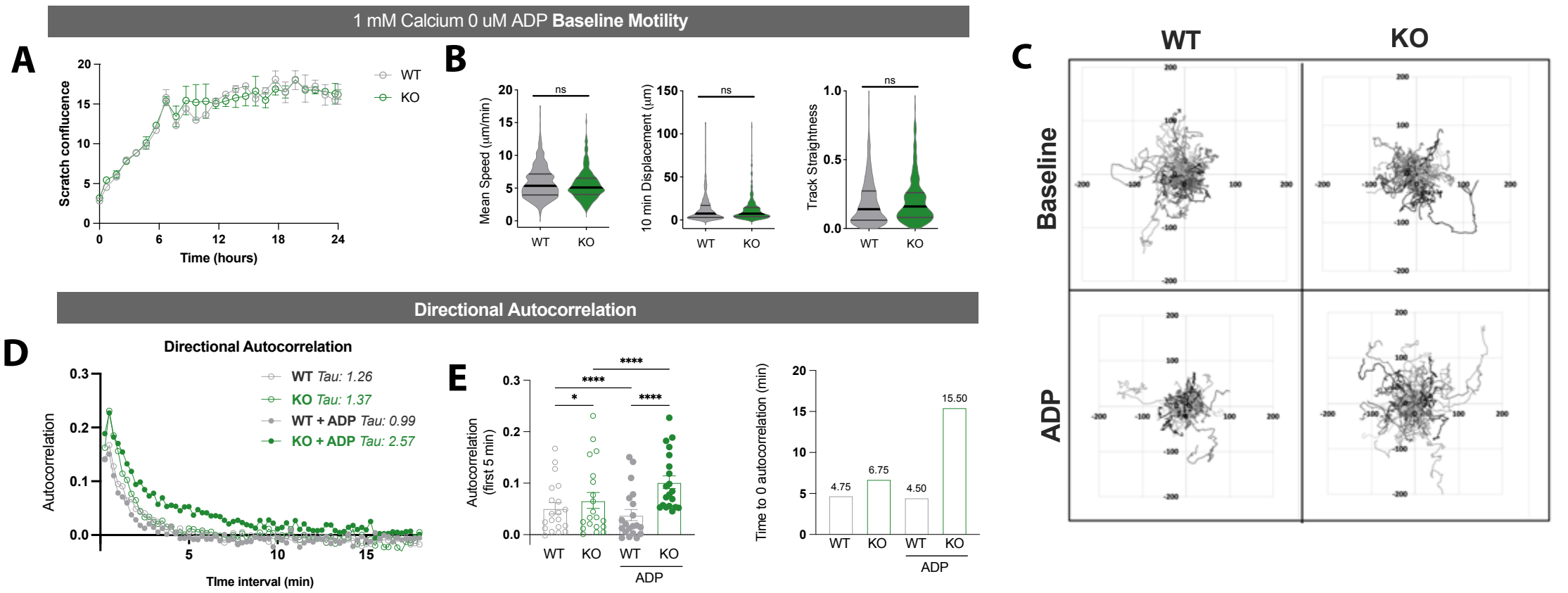

Figure 4-figure supplement 2: Comparison of process extension in WT and TREM2 KO Microglia.

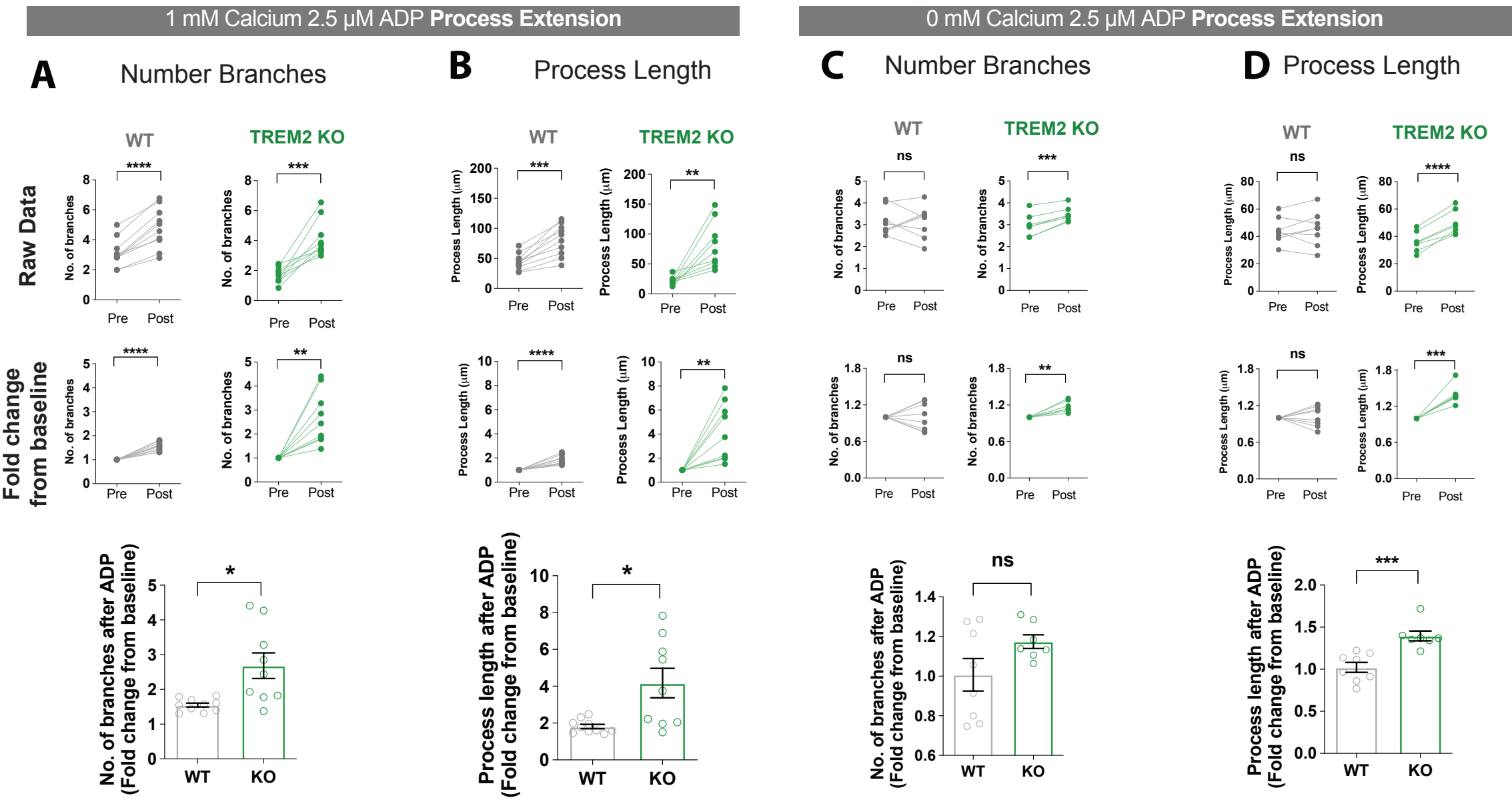

Figure 5: Validation of Salsa6f transgenic iPSC-microglia.

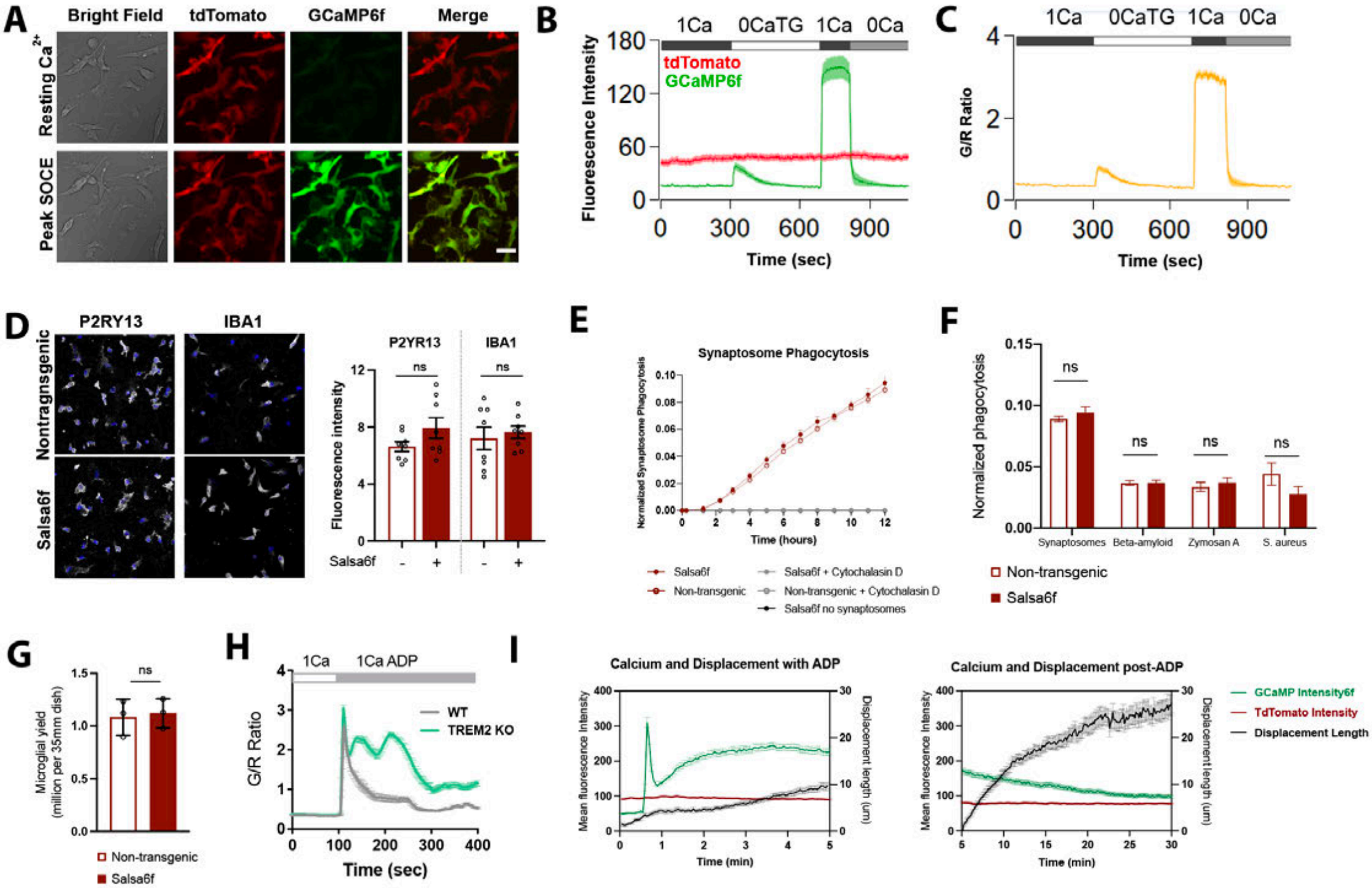

Figure 5-figure supplement 1: Generation of Salsa6f iPSC line.

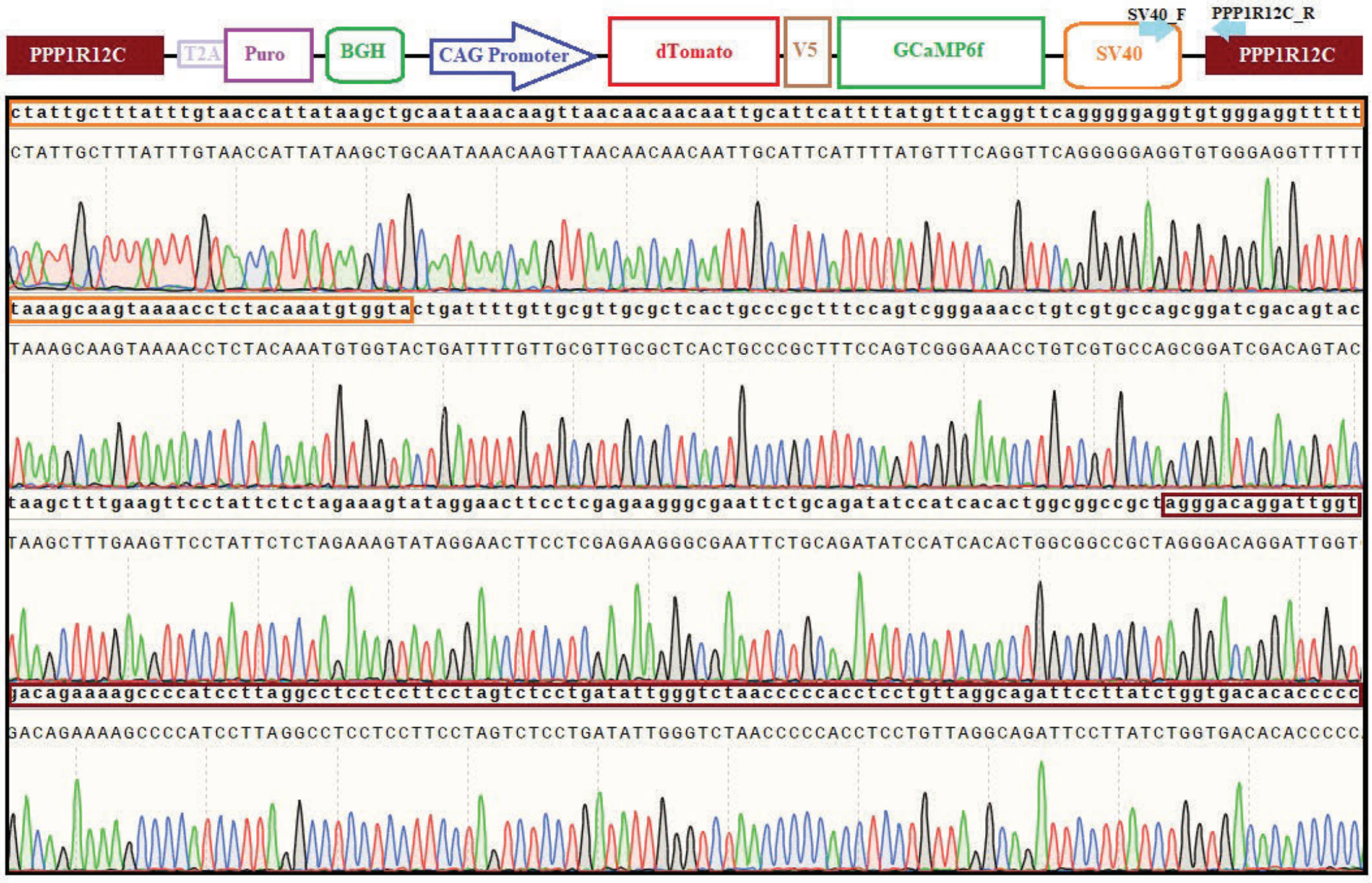

Figure 6: Cytosolic Ca^{2+} levels tune microglial motility in TREM2 KO cells.

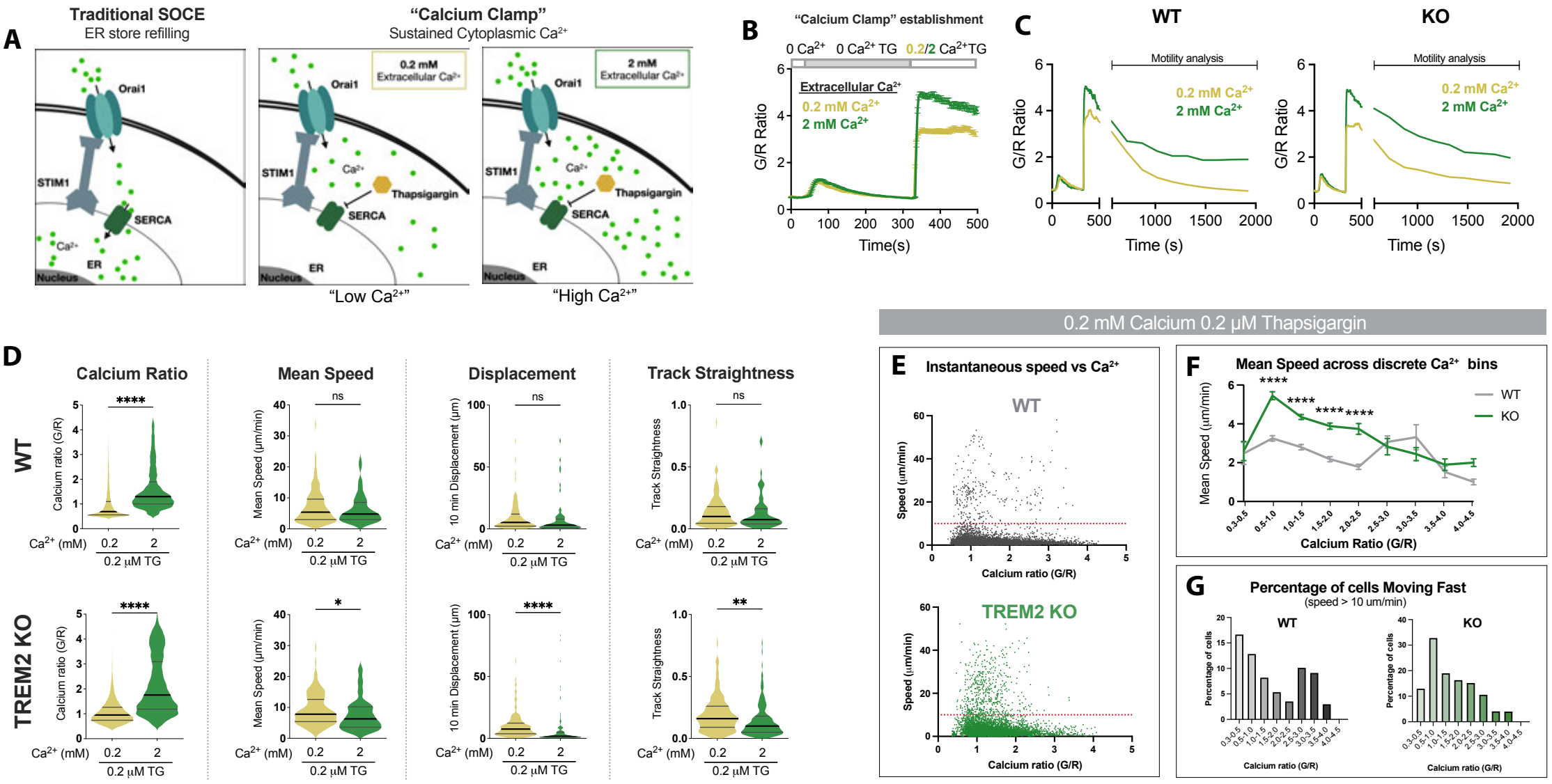

Figure 6-figure supplement 1: Motility analysis with "Ca^{2+} clamp".

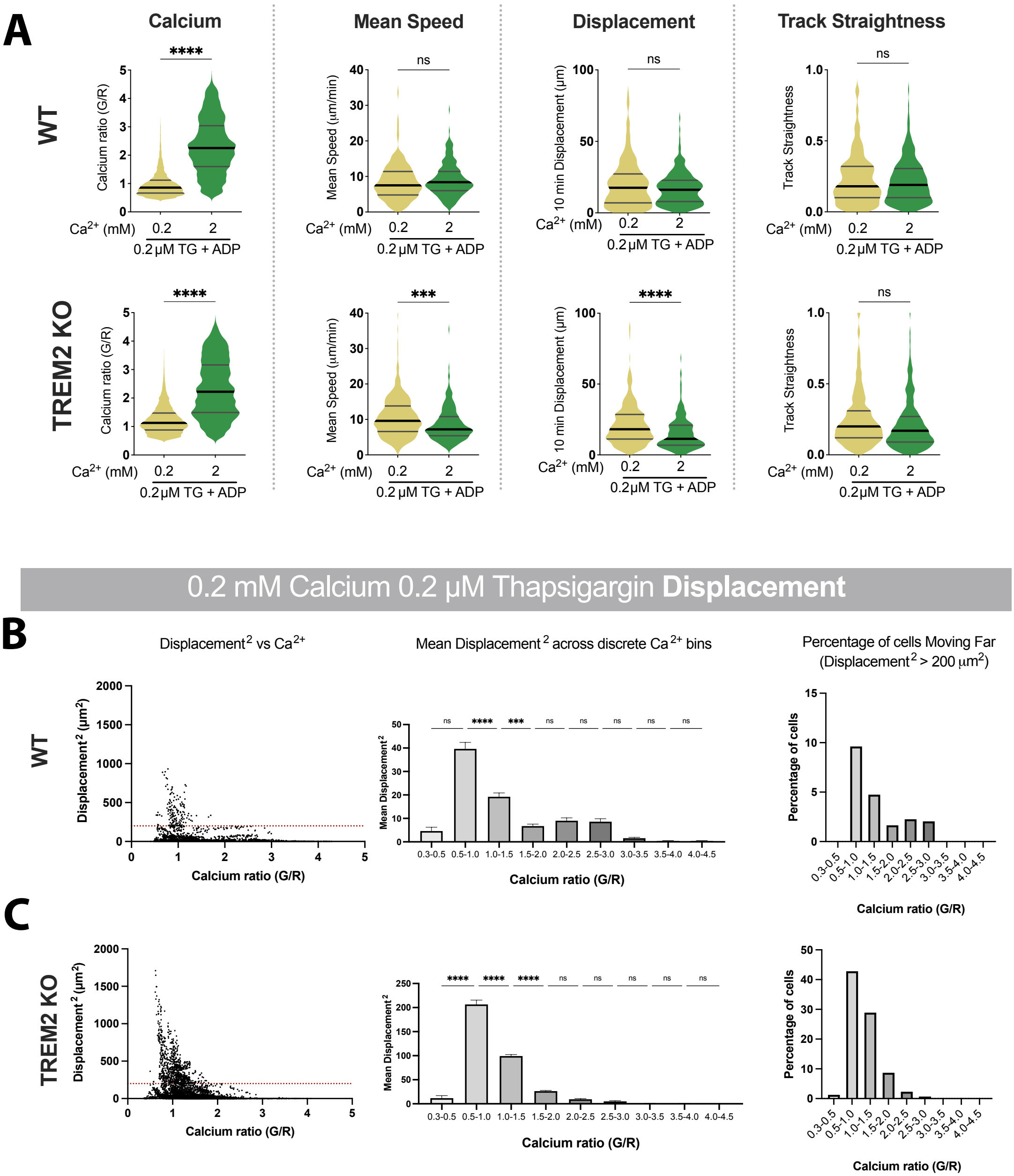

0.2 mM Calcium 0.2 µM Thapsigargin **Displacement**

Figure 7: Migration deficits in TREM2 KO microglia are rescued by inhibition of purinergic signaling.

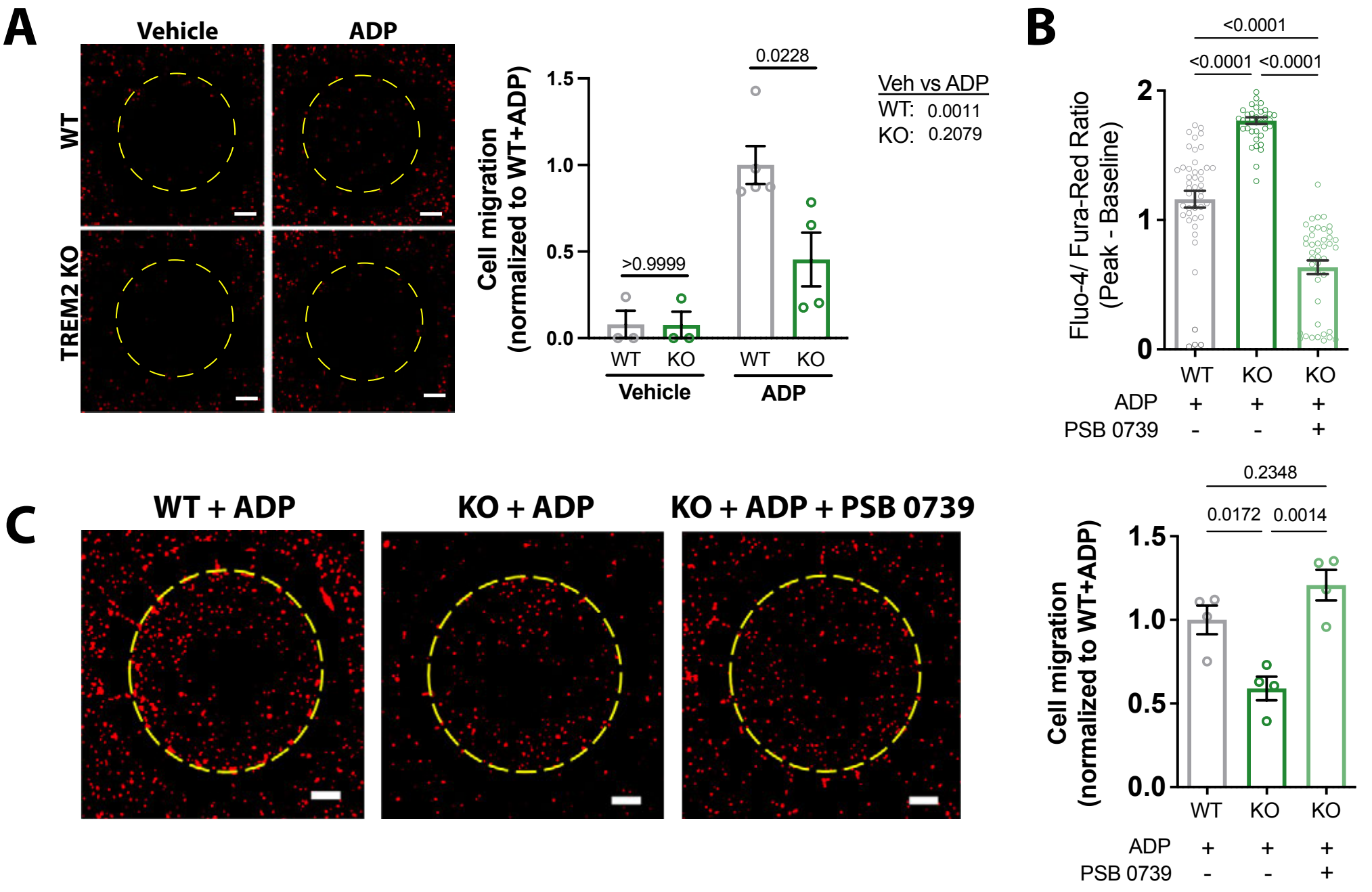
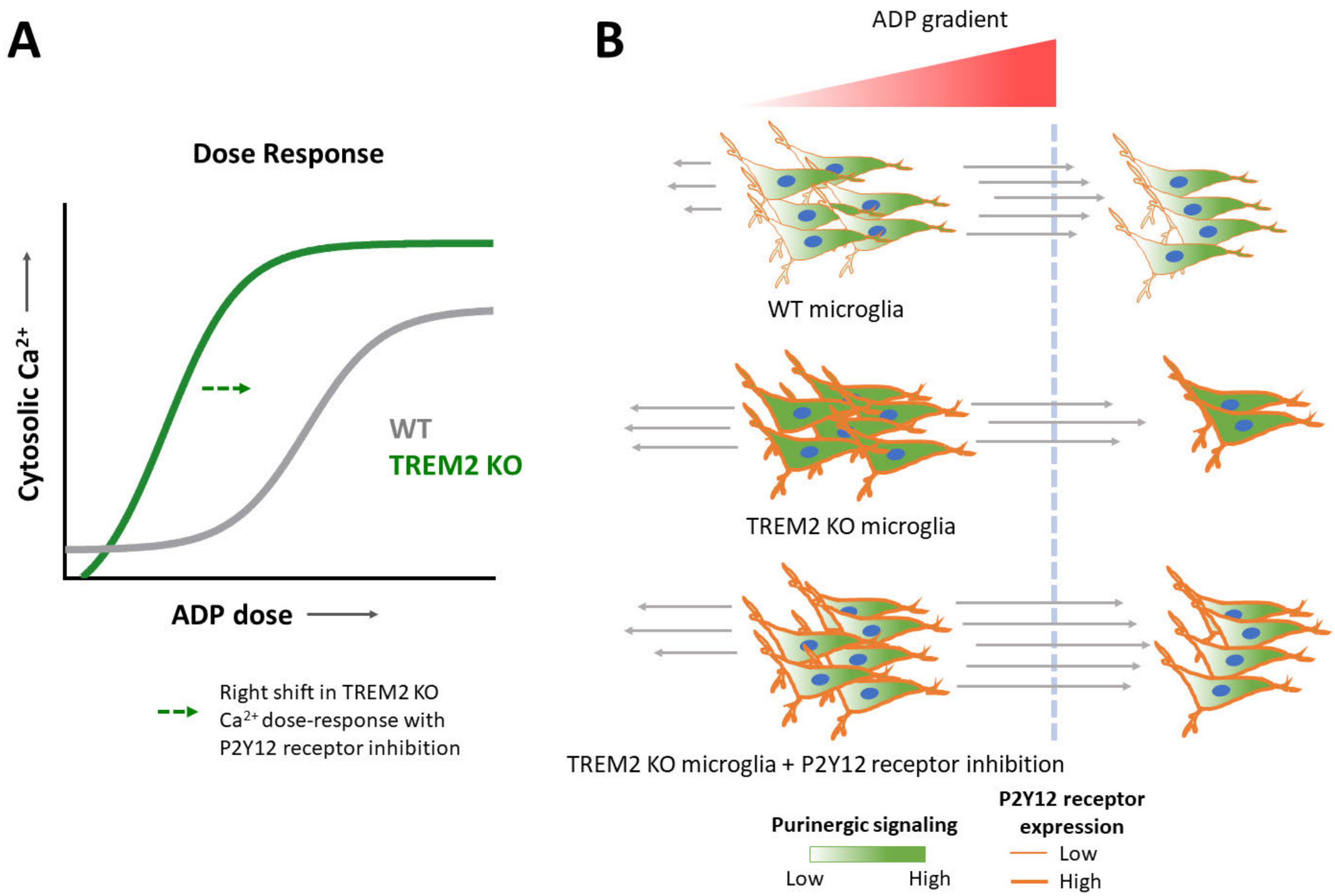
Figure 8: A Model for Ca^{2+} regulation of ADP-mediated chemotaxis in microglia lacking TREM2.